Observation of hidden atomic order at the interface between Fe and topological insulator Bi_2Te_3

PCCP

Accepted Manuscript

ROYAL SOCIETY OF CHEMISTRY

rsc.li/pccp

View Article Online
DOI: 10.1039/C7CP04875K

Observation of hidden atomic order at the interface between Fe and topological insulator Bi_2Te_3

Jaime Sánchez-Barriga[1], Ilya I. Ogorodnikov[2], Mikhail V. Kuznetsov[2], Andrey A. Volykhov[3,4], Fumihiko Matsui[5], Carolien Callaert[6], Joke Hadermann[6], Nikolay I. Verbitskiy[7], Roland J. Koch[8], Andrei Varykhalov[1], Oliver Rader[1] and Lada V. Yashina[3]

[1] Helmholtz-Zentrum Berlin für Materialien und Energie, Albert-Einstein-Str. 15, 12489 Berlin, Germany

[2] Institute of Solid State Chemistry of the Ural Branch of the Russian Academy of Sciences, Pervomayskaya Str. 91, 620990 Ekaterinburg, Russia

[3] Department of Chemistry, Lomonosov Moscow State University, Leninskie Gory 1/3, 119991 Moscow, Russia

[4] Kurnakov Institute of General and Inorganic Chemistry RAS, Leninskii prosp. 31, 119991 Moscow, Russia

[5] Nara Institute of Science and Technology, 8916-5 Takayama-cho, Ikoma, Nara 630-0192, Japan

[6] Electron microscopy for materials science, University of Antwerp, Prinsstraat 13, 2000 Antwerp, Belgium

[7] Vienna University, Faculty of Physics, Boltzmanngasse 5, A-1090 Vienna, Austria

[8] Advanced Light Source, 1 Cyclotron Road, Lawrence Berkeley National Laboratory, Berkeley, CA 94720-8229, USA

ABSTRACT

To realize spintronic devices based on topological insulators (TIs), well-defined interfaces between magnetic metals and TIs are required. Here, we characterize atomically precisely the interface between the 3*d* transition metal Fe and the TI Bi_2Te_3 at different stages of its formation. Using photoelectron diffraction and holography, we show that after deposition of up to 3 monolayers Fe on Bi_2Te_3 at room temperature, the Fe atoms are ordered at the interface despite the surface disorder revealed by our scanning-tunneling microscopy images. We find that Fe occupies two different sites: a hollow adatom deeply relaxed into the Bi_2Te_3 quintuple layers and an interstitial atom between the third (Te) and fourth (Bi) atomic layers. For both sites, our core-level photoemission spectra and density-functional theory calculations demonstrate simultaneous chemical bonding of Fe to both Te and Bi atoms. We further show that upon deposition of Fe up to a thickness of 20 nm, the Fe atoms penetrate deeper into the bulk forming a 2-5 nm FeTe interface layer. In addition, excessive Bi is pushed down into the bulk of Bi_2Te_3 leading to the formation of septuple layers of Bi_3Te_4 within a distance of ~25 nm from the interface. Controlling the magnetic properties of the complex interface structures revealed by our work will be of critical importance when optimizing the efficiency of spin injection in TI-based devices.

Keywords: topological insulator, magnetic metal, interface structure, topological surface states, photoelectron diffraction, x-ray photoelectron spectroscopy, high-resolution STEM

INTRODUCTION

For many potential applications of topological insulators[1-10] (TIs) in spintronics, detailed knowledge of the structural properties of interfaces with magnetic materials is of crucial importance. In this context, a promising and established route to explore the interaction between spin polarized topological surface states (TSSs) and magnetism is the deposition of magnetic metals on TI surfaces[11-20]. Up to date, this approach has been routinely employed to investigate the influence of the magnetic properties of the overlayer on such exotic interfaces[21-23]. Using x-ray magnetic circular dichroism (XMCD) it has been shown that Fe adatoms on Bi_2Se_3 possess a magnetic anisotropy oriented parallel to the surface plane[11], and that the resulting in-plane exchange field does not open a band gap at the Dirac point[4, 12, 24].

View Article Online
DOI: 10.1039/C7CP04875K

The latter has been demonstrated to be independent of the deposition temperature by angle-resolved photoemission (ARPES)[12].

Further XMCD studies[13] established that for ultralow Fe coverages of ~0.005 monolayer (ML) on Bi_2Te_3, the magnetization perpendicular to the surface is strongly enhanced but not sufficient to open a band gap of measurable size. This was in agreement with the very small gap predicted by theoretical calculations[14] showing that in the low coverage regime Fe spins are preferentially oriented perpendicular to the surface plane. Similarly, experiments on Co and Ni overlayers, despite the smaller magnetic moment of the latter, indicate that adatoms of prototypical ferromagnets on TIs are in general weakly hybridized with the substrate[13]. The weak hybridization observed when magnetic impurities are deposited on the TI surface differs from the impurity-mediated coupling found between bulk and surface states when the magnetic impurities are deliberately introduced into the bulk[25]. In this case, ferromagnetism[26,27] and a surface band gap opening at the Dirac point of the TSS were observed[28]; however, for Mn in Bi_2Se_3 the gap exceeded in size band structure predictions[29-32] and persisted well above the Curie temperature, pinpointing a non-magnetic origin of the gap[25]. In contrast to this, the observed robustness of the TSS against magnetic moments on the surface is a crucial precondition for the exploration and functionalization of interfaces between TIs and ferromagnets. This should also be accompanied by strategies for suppressing the bulk contribution in transport[33].

In fact, exploiting such a tolerance of TSSs against magnetic moments on the surface, for example to realize efficient spin injection in future TI-based devices, is ideal as the Dirac point and the surface-state linear dispersion would be retained together with the topological properties in the near-interface region. These are important factors to achieve high spin current densities, and for this purpose Fe is an attractive candidate material because it possesses the largest exchange splitting among the 3*d* transition metals[34-36].

However, for this to be fully realized, a comprehensive picture of the atomic structure of the interface is indispensable. The structure, in turn, depends substantially on both coverage and temperature. In this respect, the currently available data are mostly related to individual magnetic impurity atoms or point defects on the surface. In addition, previous experiments mainly concern Bi_2Se_3[11,13-15,18,37,38]. At the same time, low temperature scanning tunneling microscopy (STM) studies reveal that surface hollow adsorption sites are most favorable for Fe coverages below ~0.01 monolayer (ML)[11,18]. At room temperature, cation substitutional sites have been assumed for Fe on Bi_2Se_3[15] and Bi_2Te_3[18]. Polyakov et al.[19] have found no indication of interstitial or intercalated Fe atoms up to 0.3 ML thickness deposited on Bi_2Se_3 at 160 K. Fe replaces Bi atoms causing a substantial structural relaxation of the surrounding atoms, as well as a variation of the Fe-Se distances between 2.39 and 2.57 Å. After annealing to 520 K the formation of a α-FeSe-like structure with a local order up to the 6th shell was observed[19]. However, the atomic structure of the interface under high Fe coverages, which in the context of practical applications is also critically important, has remained largely unexplored.

In the present work, we focus on the Fe/Bi_2Te_3 interface and describe its bond geometry and morphology on the basis of X-ray core-level photoemission spectroscopy (XPS), chemical-state sensitive photoelectron diffraction (XPD) and holography (XPH) experiments. We further discuss the experimental results by comparing the atomic structure and corresponding chemical shifts obtained by density-functional theory (DFT) modelling. In particular, we use full hemisphere XPD and XPH to study local order not only for the atoms of a specific element but also for individual chemical states. We discover hidden structural order at the Fe/Bi_2Te_3 interface caused by a partial penetration of Fe atoms due to their chemical interaction with the substrate. In addition, cross-sectional transmission electron microscopy (TEM) analysis reveals that for thick Fe films an amorphous FeTe layer is formed in the interface region. We further demonstrate that excessive Bi atoms migrate into the bulk of the

View Article Online
DOI: 10.1039/C7CP04875K

crystal, causing the formation of randomly distributed Bi_3Te_4 septuple layers. The complex interface structures revealed by our work should be taken into account when designing pathways to optimize the efficiency of spin injection in future TI-based devices.

RESULTS AND DISCUSSION

Chemical interaction

To probe chemical interactions between deposited Fe and Bi_2Te_3 substrate we used core-level photoemission spectroscopy. We measured the shallow Bi 5*d*, Te 4*d* and Fe 3*p* core levels to get naturally narrowest peaks. In addition, we recorded the Fe 2*p* core level to check for a multiplet structure in the spectrum, since Fe 2*p* has much larger spin-orbit splitting than Fe 3*p*, and Fe $2p_{3/2}$ and Fe $2p_{1/2}$ do not overlap with each other.

The Fe 2*p* spectra presented in Fig. 1a for different Fe coverages on Bi_2Te_3 are essentially broader than that of a reference bulk polycrystalline Fe film. Nearly in the whole coverage range, the Fe 2*p* binding energy slightly differs from the one corresponding to the reference bulk metal, with the energy difference being less than 1.2 eV. Thus, the Fe 2*p* core levels can neither be assigned to Fe^{3+} nor Fe^{2+} substitutional atoms. However, at low Fe coverages we observe a slight indication of a multiplet splitting or additional peaks as clearly seen in the normalized spectra presented in Fig. S1 of the Supplementary Information. Moreover, the main peak position depends on the Fe coverage and shifts towards lower binding energy with increasing coverage, as clearly seen in inset of Fig. 1a. Only after deposition of 9 ML Fe, the peak position corresponds to the value of bulk Fe.

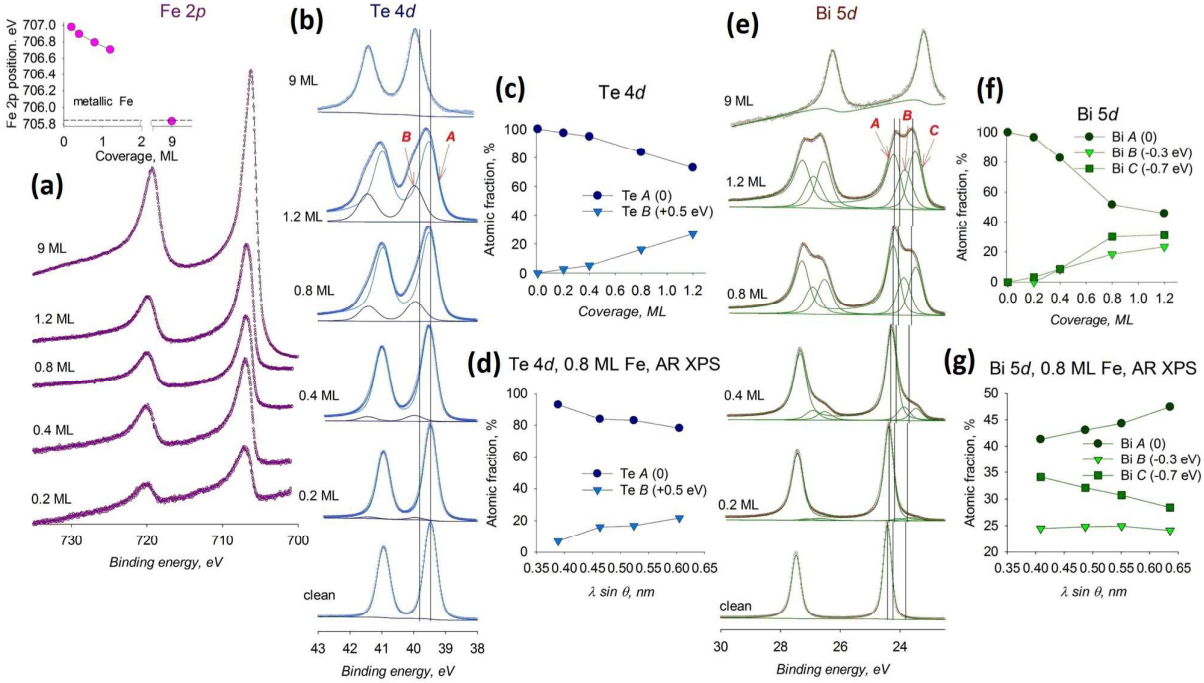

Fig. 1. Core-level photoemission spectra for the Fe-covered Bi_2Te_3 (111) surface. (a) Fe 2*p* and (b) Te 4*d* spectra as a function of Fe coverage measured with photon energies of *hv*=870 and 125 eV, respectively. (c) Relative intensity of spectral components measured as atomic fraction of the atom in the specific state in the Te 4*d* spectra shown in (b). (d) Corresponding angular dependence for an Fe coverage of 0.8 ML. (e) Similar measurements as in (b) for the Bi 5*d* core levels. (f) Relative intensity of the spectral components in the Bi 5*d* spectra shown in (e). (g) Angular dependence of the relative intensities of the Bi 5*d* spectral components after deposition of 0.8 ML Fe.

Upon Fe deposition both Bi 5*d* and Te 4*d* core-level spectra become of complex multicomponent structure, evidencing a surface chemical reaction. In the Te 4*d* spectra we observe a single broad additional component (marked as Te ***B*** in Fig. 1b). This component is

View Article Online
DOI: 10.1039/C7CP04875K

positioned at higher binding energies with the corresponding chemical shift being +0.48 eV. The relative intensity of the Te ***B*** component increases proportionally with the amount of deposited Fe, as shown in Fig. 1c. By varying the detection angle, and thus, surface sensitivity, we reveal that the Te ***B*** component corresponds to the topmost substrate layer. The detailed angular dependence is shown in Fig. 1d. All series of Bi 5*d* spectra can be fitted satisfactorily with single initial component corresponding to the clean surface (labelled as Bi ***A*** in Fig. 1e) plus two additional components (labelled as Bi ***B*** and Bi ***C***). The corresponding chemical shifts relative to bulk Bi_2Te_3 are about -0.7eV (Bi ***B***) and -0.3eV (Bi ***C***). The relative intensity of the Bi ***B*** and Bi ***C*** components progressively increases upon deposition. The angular and photon energy dependencies obtained at different coverages demonstrate the surface localization of the atoms related to the Bi ***C*** feature. An example of the angular dependence is displayed in Fig. 1g. Quantification of the surface composition at fixed electron kinetic energy indicates that the Bi to Te ratio does not change for coverages less than 2 ML, generally preserving the structure of the upper quintuple layer.

The overall behavior of the spectra is consistent with previous observations[12,20]. However, for a comprehensive interpretation of the mechanism underlying the appearance of the different spectral features, a direct theoretical modeling of the chemical shifts taking into account the possible atomic geometries is necessary, as we will discuss later.

Surface and interface structure

After deposition of 0.15 ML Fe at low temperature, as well as 0.2 and 0.4 ML Fe at room temperature on the (111) atomically flat surface of Bi_2Te_3 (illustrated as an inset in Fig. 2a), our large-scale STM images indicate that the surface is homogeneously covered with Fe, predominantly in the form of clusters, as it follows from Fig. 2. For all the deposition steps four types of structures are observed: (i) atomic defects appearing as single bright spots with a *z*-corrugation of only 1 Å and related to adatoms, (ii) dark triangles associated with substitutional atoms[14,15,37], (iii) clusters and (iv) broader islands of equal height in the order of ~2-3 nm, with their appearance depending on the Fe coverage and deposition temperature. Higher substrate temperature during deposition promotes clustering to a significant extent. Clusters dominate already after deposition of 0.4 ML Fe at room temperature. Instead, point defects prevail only at low temperature and for coverages less than ~0.1 ML; a finding which is in agreement with previous observations[11,13,18-20].

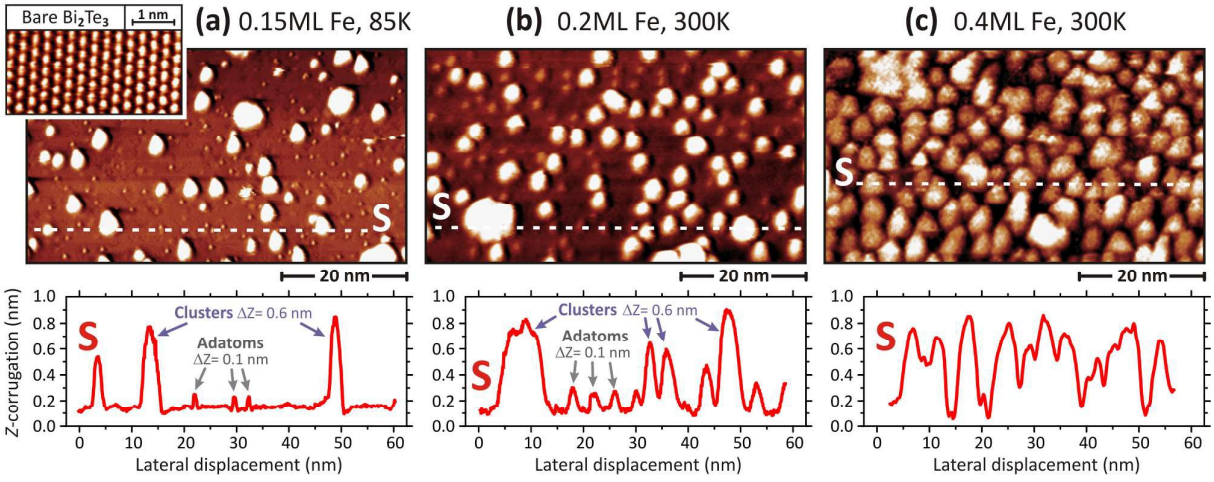

Fig. 2. STM images for the Fe-covered Bi_2Te_3 (111) surface. (a) 0.15 ML deposited at a temperature of 85 K. The inset shows the corresponding image of the clean Bi_2Te_3 surface with atomic resolution. STM images for (b) 0.2 ML Fe deposited at 300 K, and (c) 0.4 ML Fe deposited at 300K. The small Z-corrugation along the line scans marked by dashed lines in (a), (b) and (c) are given below each image.

View Article Online
DOI: 10.1039/C7CP04875K

Regarding atomic defects[11,13-15,37,38], adatoms can occupy two different hollow positions: (i) on top of Te in the third layer (structure IIa shown in Fig. S2 of the Supplementary Information) or (ii) on top of Bi in the second layer (structure IIb in Fig. S2). In both cases, the Fe equilibrium position is between the Te and Bi layers, with Fe forming chemical bonds to both Te and Bi according to our calculations. These two positions are hardly distinguishable in the STM images[13–17]. Both yield bright spots as seen in Fig. 2, but with more circular or triangular protrusion around the center of the Fe atom, in agreement with the observation in Ref. 11 and the assignment to the two different adatom positions mentioned above. It should be emphasized that the configuration of Fe on top of the Te atom is unstable.

It was established that during heating to room temperature, adatoms are transferred to substitutional positions[15,18]. The substitutional defect was found in Ref. 15 to have the lowest energy. To evaluate this, however, the system was considered without the Bi atom that was substituted. Note that in order to become substitutional the Fe atom should push the Bi atom away, meaning that Bi will move to some low-energy position. The stability of the substitutional structure strongly depends on the Bi atom position. In Ref. 15, the substitution reaction path was considered starting from the interstitial position to two stable structures of Bi at the surface – in the hollow position on top of the Fe atom (structure IIc in Fig. S2) and in the nearest hollow position (structure IId). By modelling these two structures in detail, based on interatomic distances we find that for the structure IIc the Bi-Fe interaction is still possible (2.57 Å), whereas for the structure IId the Bi atom extruded at the surface is less bonded with the corresponding Bi-Te distance equal to 3.42-3.43 Å. In STM the substitutional defects, studied also for Bi_2Se_3 doped with a small amount of Fe in the bulk[15] as well as for Fe

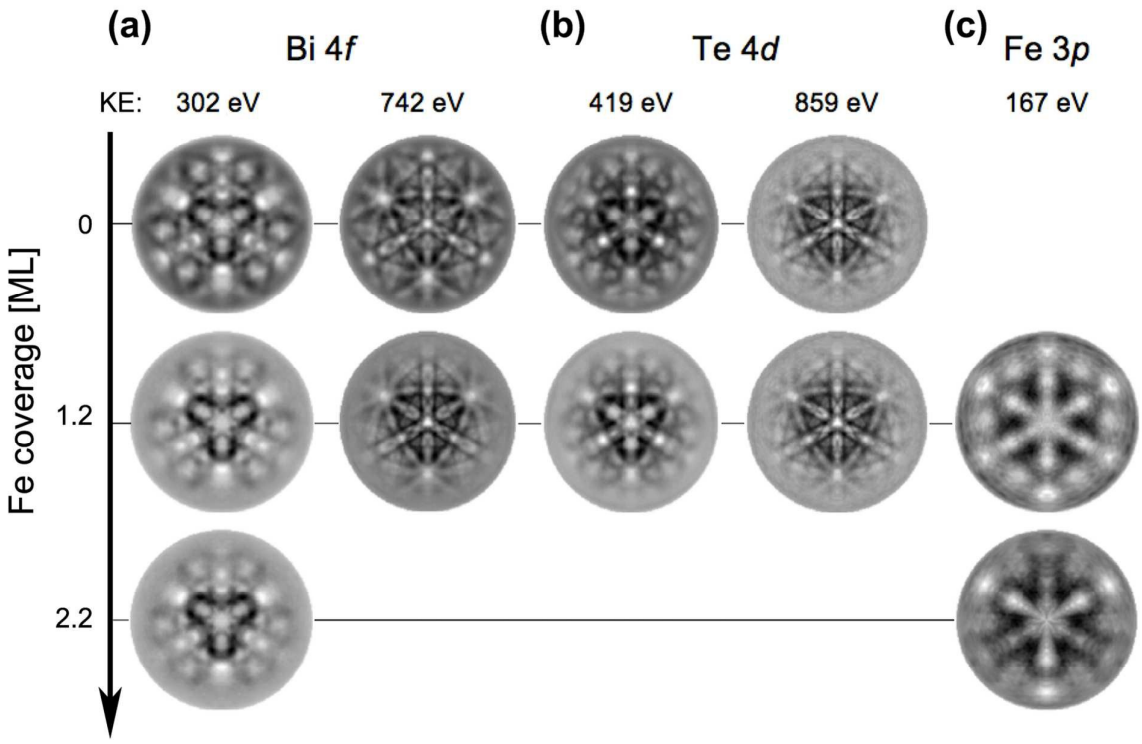

Fig. 3. Experimental photoelectron diffraction data for the Fe covered Bi_2Te_3 (111) surface. Diffraction patterns for (a) Bi *4f* , (b) Te *4d* and (c) Fe *3p* core levels as a function of increasing Fe coverage, indicated as vertical axis (from top to bottom). The kinetic energy (KE) at which the patterns where recorded is indicated on top (from left to right).

deposited both on Bi_2Te_3[15] and Bi_2Se_3[18], resemble dark triangles.

In our STM images, clusters are relatively small features exhibiting 1 nm in height and 2-3 nm in width, while islands are of much larger lateral dimensions and randomly distributed

View Article Online
DOI: 10.1039/C7CP04875K

over the surface. To understand the interface between Fe clusters or islands and the Bi_2Te_3 surface, we modeled flat Fe atomic layers (ALs) from 1 to 3 (1 AL corresponds to one Fe atom per one Te atom in the first (upper) atomic layer of the clean surface). This corresponds to 0.3-0.9 ML Fe (for details see Table S1 of the Supplementary Information). We find that for 1 AL or 0.3 ML all Fe atoms occupy hollow positions between the 1st and 2nd layers of the Bi_2Te_3 substrate. For three ALs (~ 0.9 ML), all Fe atoms are at the surface due to the formation of Fe-Fe bonds. This effect is reproducible when different starting geometries are considered (for example, 3 Fe atomic layers on top or 2 Fe layers on top plus 1 Fe layer between the Te and Bi layers). Therefore, according to our calculations one can anticipate a sharp interface below the clusters.

To investigate the interface atomic structure in more detail and to probe the atomic ordering, we used X-ray photoelectron diffraction (XPD) and holography (XPH). XPD/XPH is the most powerful tool to unravel the local atomic structure for impurity atoms[39]. The hallmark of this technique is the possibility to probe surroundings of specific atoms in their individual chemical state if the bond orientation is the same for all or at least a significant amount of atoms, with the atoms being randomly distributed.

The XPD patterns obtained for Fe coverages of 1.2 and 2.2 ML are displayed in Fig. 3. One can see that upon Fe deposition, the Bi 4*f* and Te 4*d* diffraction patterns generally remain intact, but they become less sharp especially for grazing angles. Moreover, Fe 3*p* exhibits a surprisingly pronounced diffraction pattern evidencing the preferable orientation of impurity centers, which are probably randomly distributed. It should be noted that both Fe 3*p* and Bi 4*f* patterns after 2 ML Fe deposition are less pronounced than those after 1 ML deposition. Therefore, one can assume that the ordered structure is formed at the interface only, i.e. underneath Fe islands.

To unambiguously determine the local atomic structure, we simulated the diffraction patterns for all structures related to atomic defects, i.e. for both hollow adatoms and substitutional atoms. To accurately model large agglomerates we additionally calculated different few-layered structures (see Fig. S2 of the Supplementary Information). However, note that solely based on these structures, it is not possible to fully describe the measured diffraction patterns. It should be also pointed out that neither atomic defects nor fragments of the Fe bulk structure are relevant to the measured XPD patterns.

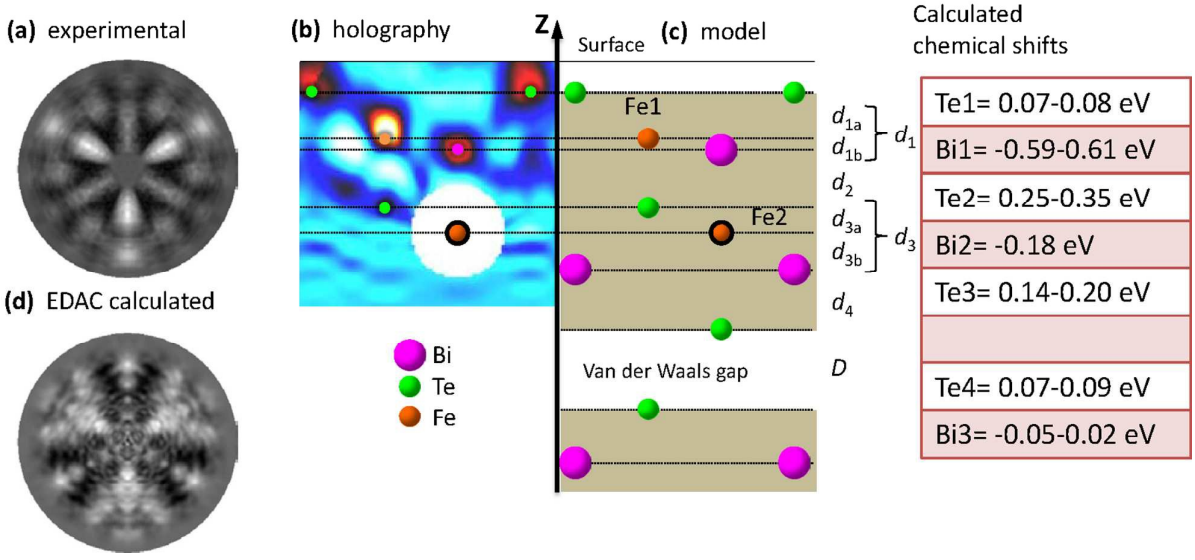

Fig. 4. Photoelectron diffraction experimental and theoretical results. (a) Fe 3*p* experimental diffraction pattern for 2.2 ML Fe on Bi_2Te_3. (b) Holography reconstruction of the Fe local environment. (c) Atomic model consistent with the results shown in (b). (d) Simulated core-level shifts for the different Te and Bi atoms in each layer obtained for the optimized structure with ¼ population of the position Fe 2. The spectral features Bi ***C*** and Bi ***B*** in Fig. 1 correspond to Bi1 and Bi2, respectively, while the spectral feature Te ***B*** to Te1+Te2+Te3 (not resolvable in the core-level spectra).

View Article Online
DOI: 10.1039/C7CP04875K

To obtain a deeper understanding of the Fe related structures we used X-ray photoelectron holography (XPH), which allows a direct reconstruction of the atomic surroundings in real space[40] and has been applied to the clean Bi_2Te_3 surface[41]. The results are illustrated in Fig. 4b. One can see four atomic layers above the Fe emitter. Unfortunately, photoelectron diffraction is not very sensitive to the chemical nature of the surrounding atoms. From typical atomic distances it can be realized that Te-Fe-Bi-Te-Fe-Bi-Te is the proper assignment of the in-depth atomic layers. In other words, Fe penetrates in the first quintuple layer and occupies two different positions, one located between the 1st and 2nd atomic layer and the other one between the 3th and 4th atomic layer. These two positions correspond to a deeply relaxed Fe adatom and an interstitial Fe atom (labelled Fe1 and Fe2 in Fig. 4c). However, the accuracy in determining the localization of the atomic positions is generally not high in XPH, further analysis is required to obtain more precise values.

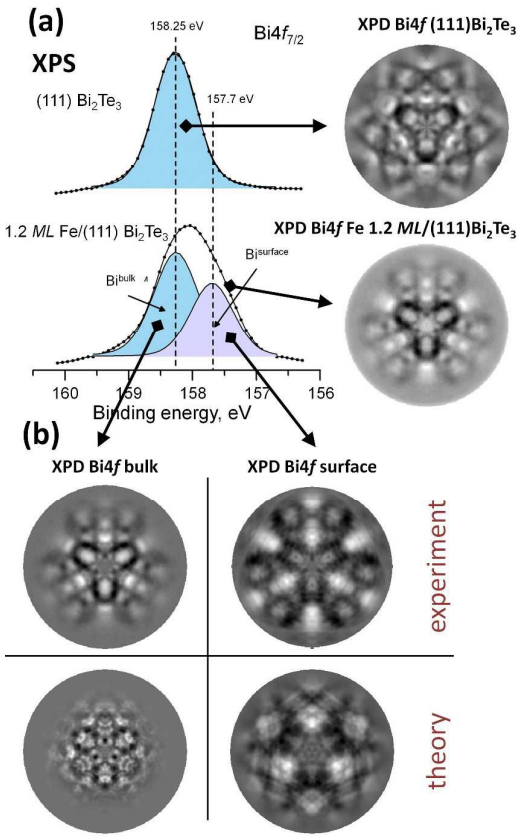

Fig. 5. Chemical state selective photoelectron diffraction. (a) Bi $4f_{7/2}$ spectra for clean Bi_2Te_3 surface (top) and after deposition of 1.2 ML Fe (bottom) and corresponding experimental diffraction patterns (right). (b) Experimental and EDAC simulated diffraction patterns for two different charge states of Bi, as decomposed in the spectrum for 1 ML Fe on Bi_2Te_3 in (a).

For this purpose, we firstly checked the stability of the most probable structure obtained from XRH data based on the DFT calculations. Here we consider 2 ALs of Fe, i.e., a coverage lower than the experimental one, taking into account that part of the Fe atoms is in clusters and does not contribute to the measured diffraction patterns. The calculated structure is found quite stable with reasonably small deviations of the interatomic distances after total optimization. The calculated structural parameters are summarized in Table 1. The main difference between the experimental structural parameters and the calculated ones is the Fe1 localization with respect to the surface, which in the calculation is less buried as compared to the experimental data. This difference is probably caused by the fact that the real system is much more complex than the modeled one, which does not include clusters or islands.

Another possibility to verify the reliability of our structural model is to compare the calculated core-level shifts for Bi 5*d* and Te 4*d* (relative to bulk Bi_2Te_3) with the experimental ones. We calculated chemical shifts and find that, indeed, Bi (Te) atoms show negative (positive) shifts. However, for Te atoms the calculated shifts are notably higher than the experimental ones. Thus, it is plausible to conclude that Fe atoms can occupy Fe2 positions only partially. Indeed for ¼ of the accessible sites the calculated core-level shifts fit well to the experimental observations (marked as blue and black vertical solid lines in Figs. 1b and 1e). The assignment of the shifts to the atomic positions is given on the right-hand side of Fig. 4c. Moreover, the highest shift in the Bi 5*d* spectra (Bi ***C*** feature) corresponds to the topmost Bi layer, a result which is consistent with the data obtained from the angular dependence shown in Fig. 1c. The Bi ***B*** feature can be assigned to the Bi2 layer. As a result, the

View Article Online
DOI: 10.1039/C7CP04875K

simulated Fe 3*p* pattern presented in Fig. 4d is in reasonable agreement with the experimental one shown in Fig. 4a.

Another set of photoelectron diffraction data was obtained for Bi 4*f* and Te 4*d* core levels. Here, we exploited the unique possibilities of chemical state selective photoelectron diffraction to determine the atomic surrounding of a specific element in different charge states, i. e. showing different chemical shifts. The Bi 4*f* spectra were fitted with two components for simplicity as presented in Fig. 5a. The two resulting diffraction patterns corresponding to the bulk and surface components shown in Fig. 5b are rather different. Both of them are in reasonable agreement with the simulated diffraction patterns as obtained using the atomic model shown in Fig. 4c.

Table 1. Interlayer parameters and ***a*** parameter for $Fe/Bi_2Te_3(111)$ surface (given in Å) obtained by photoelectron holography and photoelectron diffraction of the Fe 3*p* level compared with quantum chemical calculations (DFT) results (1 AL=0.31 ML). In DFT the value of the lateral parameter *a* was 4.46 Å after optimization of a single QL. For the bulk structure we obtained 4.43 Å.

Parameter, Å	XPH		XPD	DFT		
	Fe 1.2ML	Fe 2.3ML	Fe 2.3ML	1.25 AL	1.5 AL	2 AL
d_{1a}	1.50 ± 0.05	1.60 ± 0.05	1.62 ± 0.02	1.29	1.21-1.27	1.20
d_{1b}	0.40 ± 0.05	0.40 ± 0.05	0.34 ± 0.02	0.68	0.52-0.83	0.74
d_2	2.10 ± 0.05	2.00 ± 0.05	1.96 ± 0.02	2.01	1.83-2.20	1.97
d_{3a}	0.70 ± 0.05	0.90 ± 0.05	1.00 ± 0.02	0.96	1.06-1.16	0.91
d_{3b}	-	-	1.00± 0.05	1.16	0.85-1.25	1.14
d_4	-	-	-	1.77	1.34-2.00	1.74
D	-	-	-	-	-	2.70
a	4.40 ± 0.10	4.40 ± 0.10	4.34 ± 0.02	4.46	4.46	4.46

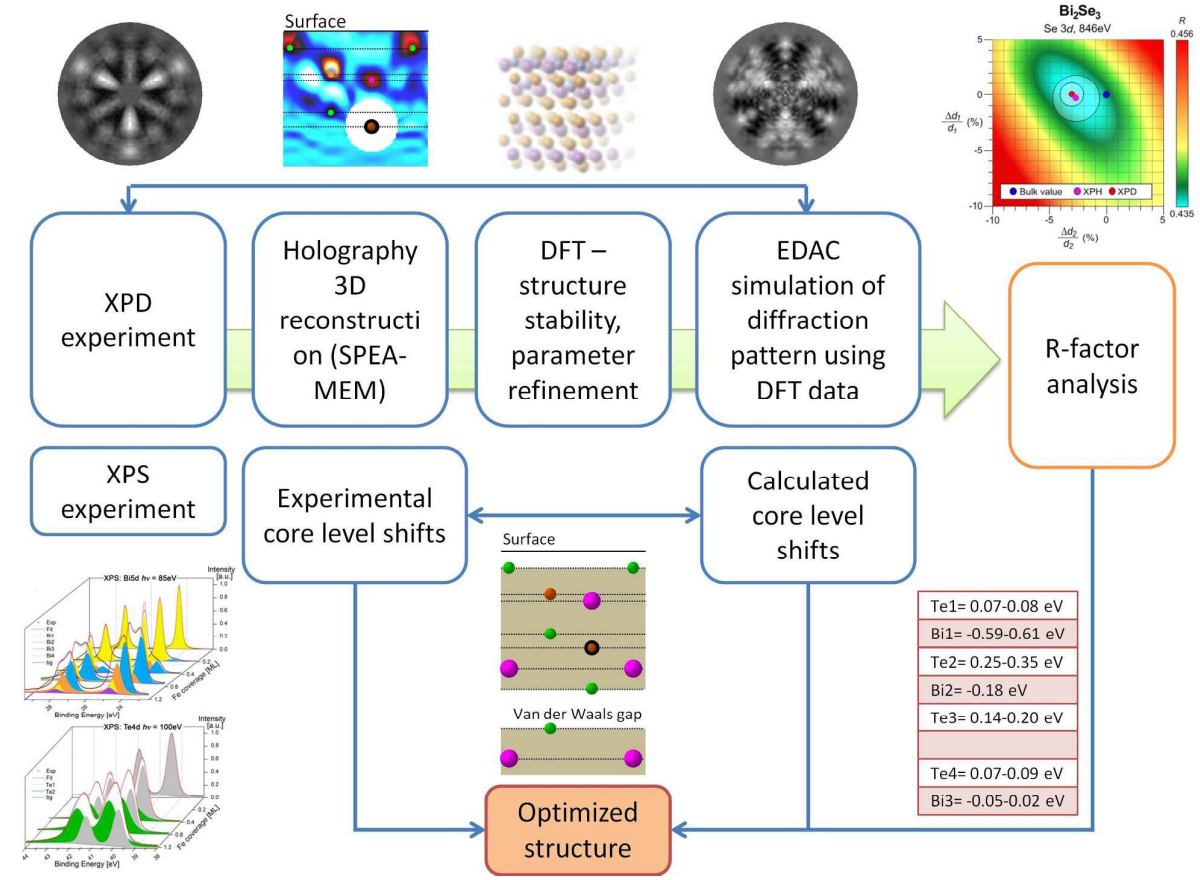

Fig. 6. Overview of the procedure used in the present work. The scheme illustrates a paradigm to determine the local structure of foreign atoms at the interface using full hemisphere photoelectron diffraction data.

View Article Online
DOI: 10.1039/C7CP04875K

The most accurate structural information from the experiment can be obtained from XPD by an *R*-factor analysis as described in the Methods section. The corresponding atomic geometry parameters are summarized in Table 1.

An illustration of our new approach to discover the atomic structure of the shallow interface is presented in Fig. 6. It includes the analysis and assessment of different kinds of experimental data. Based on photoelectron holography of the impurity atom emitter the local environment is reconstructed in real space by XPH, then the structure is tested for stability by DFT, and further verification is reached using chemically state selective Bi 4*f* XPD as well as by comparing the calculated and experimental core-level shifts. For the structure obtained in this way, the XPD pattern is simulated accordingly, with the corresponding structural parameters being optimized by *R*-factor analysis. Using this paradigm, our results unambiguously demonstrate that after few-layer deposition of Fe on the Bi_2Te_3 (111) surface, there is hidden atomic order at the very interface, in spite of the surface disorder revealed by our STM images. Our atomic structure includes two possible sites of Fe atoms with different occupancy, one corresponding to a highly populated adatom position and the other one to a less populated interstitial position. We believe that this specific structure is responsible for the behavior of the electronic structure observed in Ref. 42.

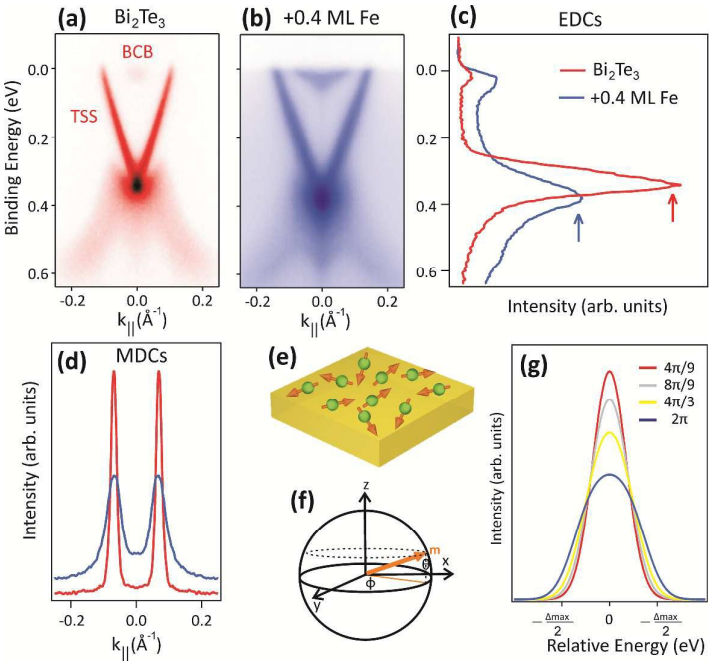

Fig. 7. Influence of Fe deposition on the electronic structure of Bi_2Te_3. (a) ARPES dispersion of clean Bi_2Te_3 measured at a photon energy of $h\nu$ =55eV at room temperature. (b) Corresponding ARPES dispersion after deposition of 0.4 ML Fe. The intensity contribution from the bulk-conduction band (BCB) near the Fermi level and the TSS are clearly seen. (c) EDCs extracted from (a) and (b) at $k_{||}$=0. (d) Corresponding MDCs extracted at 0.2 eV above the Dirac point. (e) Schematic of Bi_2Te_3 with Fe magnetic impurities on the surface. (f) Representation of Fe magnetic moment in three-dimensions. (g) Calculated spectral weight at the Dirac point for different constraints in the orientation of the Fe magnetic moments within a range of solid angles. The constraints correspond to symmetric polar angles below 45° with respect to the x-y plane, which add up to the total solid angle indicated in the legend.

In this respect, we have analyzed the energy-momentum band dispersions of the TSS upon Fe deposition up to 0.4 ML at room temperature using ARPES (see Fig. 7). For the pristine Bi_2Te_3 sample (Fig.7a), the Dirac point appears with high intensity at a binding energy of ~0.34 eV, and clearly shifts towards higher binding energy by about 40 meV after deposition of 0.4 ML Fe (Fig. 7b). In addition, the shift is accompanied by a clear suppression of both the Dirac point spectral weight and the intensity of the TSS bands, as well as by an additional broadening of the bands that appears very pronounced from the Dirac point up to the Fermi level. In Fig. 7c we compare the broadening and intensity of Dirac point as extracted from energy-distribution curves (EDCs) at zero momentum ($k_{||}$=0) before (red) and after Fe deposition (blue). Correspondingly, in Fig. 7d we compare the additional broadening of the Dirac bands as seen in momentum-distribution curves (MDCs) for the pristine sample (red) and 0.4 ML Fe/Bi_2Te_3 (blue). It is in principle possible to consistently reconcile both effects,

View Article Online
DOI: 10.1039/C7CP04875K

i.e. the intensity suppression of the Dirac point and the additional broadening with a magnetic anisotropy of the Fe preferentially oriented parallel to the surface. Note that under this configuration no band gap at the Dirac point is expected in agreement with our observations.

Nevertheless, we developed an ergodic model to simulate the spectral weight in the vicinity of the Dirac point assuming Fe magnetic moments mainly oriented parallel to the sample surface (Fig. 7e). In our model, canted magnetic moments introduce a gap which varies in size from zero to Δ_{max} depending on the magnitude of their out-of-plane component[43] (Fig. 7f). For simplicity, we have not considered the additional smearing of the Dirac point intensity along the momentum direction due to the in-plane projection of the Fe magnetic moments, which is responsible for the additional broadening observed in Fig. 7c. We represent the electronic bands by Gaussian peaks with a full-width at half-maximum which is about 30% of the maximum value of the band-gap size located symmetrically with respect to the Dirac point when the gap opens. Note that the model works for any possible generic value of Δ_{max} which is expected to be small[29-32]. Figure 7g depicts the evolution of the spectral weight at $k_{||}$=0 for configurations where the magnetic moments are restricted to polar angles θ around the *x*-*y* plane (colored lines). The curves correspond to magnetic moments constrained by symmetric polar angles with respect to the *x*-*y* plane which add up to the total solid angle indicated in the legend. We clearly observe that constraining the magnetic moment to polar angles θ below 45° smears the intensity along the energy axis, in agreement with the experiment.

We have to stress that in ARPES, static magnetic moments pointing mainly parallel to the surface plane within the probed area, but some of them with a small canting, can be viewed as a superposition of different photoemission signals that are spatially averaged (gapped *vs*. non-gapped states). As canted magnetic moments will introduce a very small gap which varies in size depending on the magnitude of their perpendicular component[43], most of their contributions to the ARPES intensity will be concentrated near the Dirac point. Therefore, from the additional broadening of the Dirac peak in the EDC of the Fe covered surface in Fig. 7d, which amounts to ~50 meV, we can estimate after deconvolution of the spectrum a maximum possible gap of ~20 meV.

Interface structure in the bulk limit

Questions arise concerning the evolution of the interface structure upon deposition of thicker Fe films. To investigate this, we used high-resolution scanning transmission electron microscopy (STEM) and found that deposition of thick Fe films in the form of a compact layer results in a modification of the interface structure. The structure obtained after deposition of a 20 nm Fe layer was studied with HAADF-STEM on a cross-sectional sample (see Fig. 8). The Fe layer is found to be crystalline. All Fourier

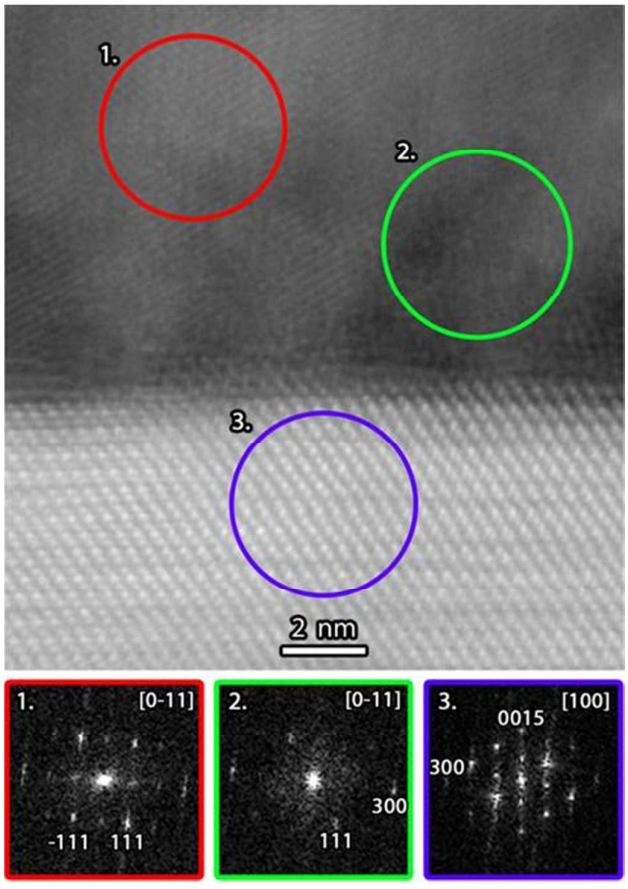

Fig. 8. Characterization of the interface structure for 20 nm thick Fe on Bi_2Te_3 using high-resolution STEM. (Top) Cross-sectional HAADF-STEM image. (Bottom) Corresponding Fourier transforms obtained from the green, blue and red regions labelled from 1 to 3, respectively.

View Article Online
DOI: 10.1039/C7CP04875K

transforms of different areas of the STEM image (bottom panels of Fig. 8) extracted from some regions (labelled 1 and 2 in red and green color, respectively) within the Fe layer can be indexed using cell parameters $a=b=c=3.5 \pm 0.1$ Å. There are random distortions from the $Fm3m$ structure as one would expect for bulk Fe with these cell parameters. For example, in the Fourier transform of region 1, the reflections correspond to a primitive cell rather than to a *F*-centered one. On the other hand, in the case of region 2 only few reflections can be obtained. The angle between the *c*-axis of Bi_2Te_3 and the (111) direction of the Fe lattice comprises 25°-30°.

Just below the Fe layer an amorphous layer (≈3.5 nm) mostly consisting of Te and Fe is formed as demonstrated in Fig. 9 by the interface morphology seen in the STEM images, as well as by the corresponding depth profiles obtained using energy-dispersive X-ray (EDX) nanoprobe analysis shown in Fig. 10. The STEM images displayed in Fig. 9 also show that the top layer of the substrate consists of a mixture of quintuple (Bi_2Te_3, Te-Bi-Te-Bi-Te) and septuple layers (Bi_3Te_4, Te-Bi-Te-Bi-Te-Bi-Te)[44]. The septuple layers are mostly localized within a distance of ~25 nm from the interface. This is consistent with the EDX observation evidencing a Bi/Te ratio notably higher than 2:3. This ratio is displayed as a light-blue curve in the corresponding depth profile shown in the bottom panel of Fig. 10. The excessive Bi arising as a consequence of the FeTe layer formation is forced back into the bulk, forming septuple layers. In addition, the depth profile reveals the presence of minor amounts of Fe in the top layer of the substrate which decrease rapidly over the next 6 nm.

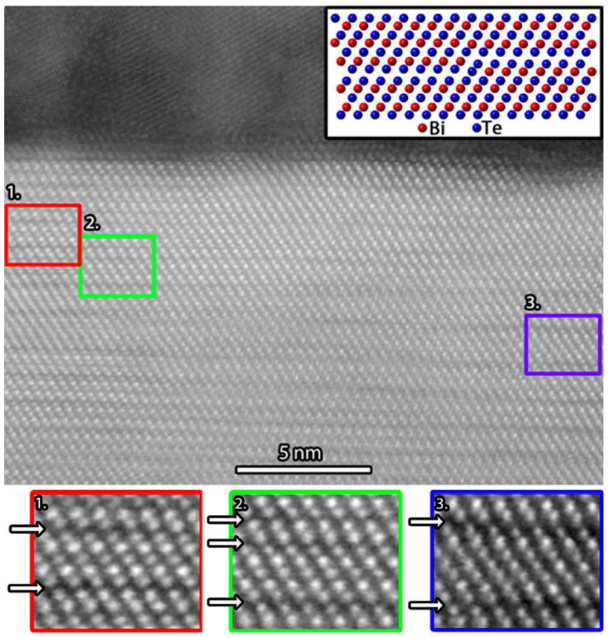

Fig. 9. Details on the interface structure of 20 nm Fe on Bi_2Te_3. The top Bi_2Te_3 layer is shown with enlargements of three indicated areas. Red (1): quintuple layer; green (2): quintuple layer with a double layer; blue (3): septuple layer. The arrows mark the Van der Waals gaps. The inset on the top right shows the transition from a quintuple layer to a septuple layer, using the model proposed in Ref. 41.

Exact visualization of these Fe positions with EDX or HAADF-STEM was hardly possible. This indicates that the Fe atoms show no long-range order over the structure and thus give too low signal in the possible individual positions, as the Fe positions along the whole thickness of the column are not completely occupied. The latter is due to the large difference between the atomic numbers of Fe and Bi or Te. A quantitative treatment of the HAADF-STEM images to derive the exact amount of Fe per column was difficult to achieve due to the mixture of quintuple and septuple layers along the projection direction. For the 20 nm textured Fe layer grown on Bi_2Te_3 (111), the interface structure contains a ≈3.5 nm amorphous FeTe interface layer, with excessive Bi migrating to the shallow bulk and forming septuple layers of Bi_3Te_4 that are randomly distributed within approximately 25 nm in depth from the interface.

CONCLUSIONS

To summarize, we studied the Fe/Bi_2Te_3 interface formation in a wide range of thicknesses starting from the sub-monolayer regime up to the bulk limit. We applied a comprehensive approach using multiple techniques combined with density-functional theory calculations. At the atomic level, interface reactions are observed which reveal a clear tendency towards the formation of a stable FeTe layer. After deposition 1-3 ML Fe at room temperature, which exhibits typical atomic defects, cluster and islands at the Bi_2Te_3 (111) surface we observed

View Article Online
DOI: 10.1039/C7CP04875K

clear ordering of the Fe atoms at the interface. We discovered the local structure in which Fe atoms occupy two different positions: hollow adatom positions deeply relaxed into quintuple layers of Bi_2Te_3 and interstitial position between third (Te) and fourth (Bi) atomic layer. We also revealed the impact that Fe deposition has on the electronic structure, and discussed the underlying mechanism giving rise to the observed suppression of the Dirac point intensity and extra broadening of the TSS bands. Finally, for the interface obtained after deposition of a 20 nm thick bulk Fe layer we directly observed the 2-5 nm FeTe interface layer, with excessive Bi migrating to shallow bulk and forming septuple layers of Bi_3Te_4.

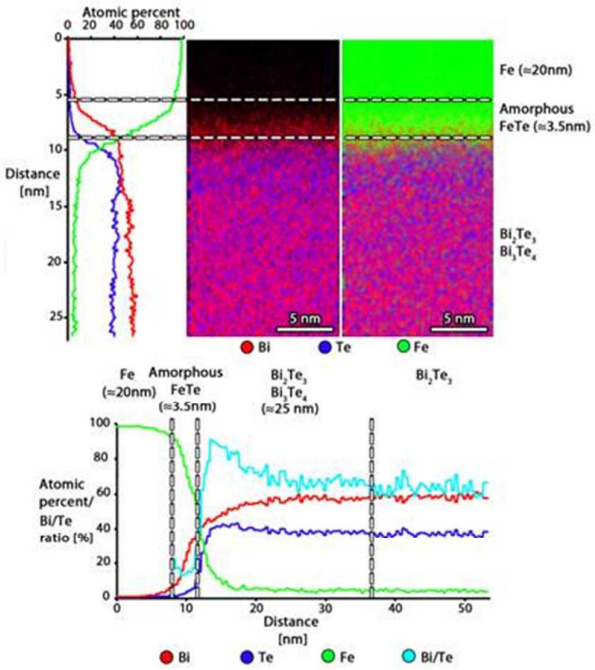

Fig. 10. Interface composition of 20 nm Fe on Bi_2Te_3. (Top) STEM–EDX maps and corresponding line profiles. (Bottom) Line profiles taken over a larger depth emphasize the deviation of the Bi:Te ratio in the top layer and the regularization of this ratio when going deeper into the bulk.

METHODS

Bi_2Te_3 *n*-type single crystals were grown using the Bridgman method[45]. The single crystals were cleaved *in situ* under ultrahigh vacuum for the ARPES, XPS, and XPD measurements. The high crystal quality of the obtained (111) Bi_2Te_3 surface was verified by low-energy electron diffraction (LEED) as well as the presence of sharp features in the ARPES dispersions. Fe was deposited *in situ* from an *e*-beam evaporator with the sample kept at the cleavage temperature. The evaporation rate was repeatedly calibrated with a quartz microbalance and was typically of the order of 0.05 monoatomic layers (ML) per minute. Faster and slower depositions did not show any influence on the results.

Photoemission experiments were carried out using several facilities of Helmholtz-Zentrum Berlin. The ARPES experiments were performed in an ultrahigh vacuum chamber with a base pressure below 1×10^{-10} mbar using a Scienta R8000 electron analyzer at the UE112/ PGM2a beamline of the synchrotron BESSY II using p-polarized undulator radiation. High-resolution XPS spectra were recorded with high surface sensitivity (i.e., the kinetic energy of the photoelectrons was set between 50 and 200 eV) at the Russian-German beamline of BESSY II. The XPS acquisition was performed using a SPECS Phoibos 150 electron energy analyzer at variable detection angles. The photoelectron diffraction patterns were taken at the U49/PGM1 beamline of BESSY II using a toroidal electron energy analyzer[46].

To simulate our photoelectron-diffraction patterns, we used the electron diffraction in atomic clusters (EDAC) software package[47]. The code is based on a multiple- scattering cluster approach, where the surface is represented by a sufficiently large number of atoms surrounding the emitter. We have performed simulations on parabolic clusters containing ~1500–1900 Bi, Fe and Te atoms within a radius of 30 Å. For each emitter, which was placed in the center, we used an individual parabolic cluster. In all calculations we considered emitters belonging to the first topmost quintuple layers.

Multiple elastic scattering of photoelectrons was modeled using a stable iterative technique until convergence was achieved. The calculations were performed for a temperature T = 300 K. Thermal vibrations were simulated using nonzero Debye temperatures for the Bi, Fe and Te

View Article Online
DOI: 10.1039/C7CP04875K

atoms: θ^{Bi}, θ^{Fe}, and θ^{Te}. By varying the radius of the parabolic clusters R_{max}, the electronic surface position z_{surf}, the Debye temperatures θ_d, the order of multiple scattering n, the inelastic mean free path, the number of emitters, as well as other parameters, the best agreement between experiment and simulation was obtained.

We used the standard procedure for structure refinement in x-ray analysis, which is the least-squares optimization using the expansion method[48]. Starting with an arbitrary structure the refinement converges to a local extremum (usually, but not necessarily, a minimum) of the *R*-factor in the parameter space. It is clear that the starting geometry should be sufficiently close to the real structure. A very rough estimate is that the atoms should be within a few tenths of an Angstrom from the correct positions. If all the atoms are misplaced, it is often not possible to start the full simultaneous refinement of all parameters. One then tries to first refine single parameters or blocks of parameters keeping other parameters fixed, and to proceed stepwise in this way until in the final step all parameters can be freed. For large structures in particular, a block refinement can be used, which however converges more slowly, or constraints can be used to move rigid groups of atoms (layers) or molecules in the structure. In any case, one must check that the same minimum is reached when starting with several different trial structures. The radius of convergence may be larger for single atoms if the major part of the starting model is correct. In general, many cycles of iteration steps are necessary to locate the true minimum of the *R*-factor. To obtain a quantitative value for the agreement between the calculated and the measured diffraction patterns R-factor analysis was used. We defined the R-factor[49] as

$$R = \frac{\sum_n (\chi_n^{th} - \chi_n^{exp})^2}{\sum_n \left[(\chi_n^{th})^2 + (\chi_n^{exp})^2 \right]} \quad (1)$$

where χ is the anisotropy of the angular intensity

$$\chi(\theta, \varphi, k) = [I(\theta, \varphi, k) - I_0(\theta, k)]/I_0(\theta, k)$$

and $I_0(\theta, k)$ is an average value of the intensity for each polar angle

$$I_0(\theta, k) = \frac{1}{N} \sum_i^N I(\theta, \varphi_i, k).$$

X-ray photoelectron holography (XPH) was used to reconstruct three-dimensional (3D) images of the atomic structure around the emitter atom from the measured XPD patterns. The calculation was performed using the scattering pattern extraction algorithm with the maximum entropy method[40]. The reconstruction algorithm does not utilize the Fourier transformation, thus allowing us to obtain the atomic arrangement without the use of a multi-energy format. To suppress image artifacts the algorithm uses the translational symmetry of the crystal in the lateral plane, namely, the unit-cell parameter as well as the real and reciprocal space filtration.

Theoretical modeling of the surface relaxation was performed within the density-functional theory approach using the projected wave generalized gradient approximation method as provided by the Vienna *ab initio* simulation package (VASP)[50,51]. Core electrons were omitted by using the standard projector augmented wave pseudopotentials. In all simulations, a (5 × 5 × 1) k-point mesh of the first Brillouin zone was used and no superlattice was employed. The parameters of the hexagonal lattice unit cell were fixed to their calculated bulk values, while the positions of all atoms were varied. The modeling was performed without any particular assumption on the Fe magnetic order. We nevertheless checked the magnetic order for the structure of Fig. 4c and found that antiparallel coupling between the Fe magnetic moments is the less preferred situation, as this configuration is less stable by about 30 meV in the simulations. For all the calculations we used slabs with one to five quintuple layers; thicker slabs change the interatomic distances by less than 0.01 Å. Core-level shifts were calculated in the initial-state approximation as a variation of the electrostatic potentials at the atomic

View Article Online
DOI: 10.1039/C7CP04875K

centers as described in Ref. 52.

For high-angle annular dark field scanning transmission microscopy (HAADF-STEM) imaging and EDX mapping, cross sectional samples were prepared on a Cu and a Be support with focused ion beam (FIB) milling. A transfer module from Kammrath and Weiss GmbH was used to keep the sample in inert Ar gas during transport. Two platinum layers were deposited on the material to protect it from damage during preparation, an electron beam deposited Pt layer followed by an ion-beam deposited Pt layer. The HAADF-STEM and EDX data were acquired on aberration-corrected FEI Titan transmission electron microscopes operating at 300 kV, one of which is equipped with a Super-X detector. To limit air exposure, the samples were mounted in the holder in a glove box filled with inert Ar gas. The sample was transported in an inert atmosphere and was only exposed to air shortly before and after Ar plasma cleaning.

CONFLICT OF INTERESTS

There are no conflicts of interest to declare.

AUTHOR CONTRIBUTIONS

Jaime Sánchez-Barriga and Lada V. Yashina performed ARPES studies. Ilya I. Ogorodnikov, Mikhail V. Kuznetsov, Roland J. Koch and Fumihiko Matsui performed photoelectron diffraction studies. Nikolay I. Verbitskiy and Andrey A. Volykhov carried out XPS experiments and DFT modelling. Andrei Varykhalov performed STM experiments. Carolien Callaert and Joke Hadermann conducted TEM studies. Jaime Sánchez-Barriga, Oliver Rader and Lada V. Yashina conceived and coordinated the project. Jaime Sánchez-Barriga and Lada V. Yashina wrote the manuscript with input from all authors.

ACKNOWLEDGMENTS

The authors acknowledge financial support within the bilateral program “Russian-German Laboratory at BESSY II” and thank Helmholtz Zentrum Berlin for granting access to the beamlines RGBL, UE112-PGM2a and U49-PGM1. The Supercomputing Center of Lomonosov Moscow State University is gratefully acknowledged for granting access to the “Lomonosov” supercomputer. The work was partially supported by DFG priority program SPP 1666, Impuls- und Vernetzungsfonds der Helmholtz-Gemeinschaft (Grant No. HRJRG-408) and Russian Foundation for Basic Research (Grants No. 13-02- 91327 and No. 16-29-06410). A.P.S. acknowledges support from the German-Russian Interdisciplinary Science Center of Excellence. C. C. acknowledges support from the University of Antwerp through the BOF grant 31445. The authors thank Dr. Vera Neudachina, Daria Tsukanova, Elmar Kataev and Dr. Maria Batuk for their support during the XPS and TEM experiments.

Biblioghaphy

(1) Kane, C. L.; Mele, E. J. Z 2 Topological Order and the Quantum Spin Hall Effect. *Phys. Rev. Lett.* **2005**, *95*, 146802.

(2) Hasan, M. Z.; Kane, C. L. *Colloquium* : Topological Insulators. *Rev. Mod. Phys.* **2010**, *82*, 3045–3067.

(3) Fu, L.; Kane, C. L.; Mele, E. J. Topological Insulators in Three Dimensions. *Phys. Rev. Lett.* **2007**, *98*. 106803.

(4) Moore, J. E.; Balents, L. Topological Invariants of Time-Reversal-Invariant Band Structures. *Phys. Rev. B* **2007**, *75*, 121306(R).

(5) Murakami, S. Phase Transition between the Quantum Spin Hall and Insulator Phases in 3D: Emergence of a Topological Gapless Phase. *New J. Phys.* **2007**, *9*, 356–356.

(6) Hsieh, D.; Xia, Y.; Wray, L.; Qian, D.; Pal, A.; Dil, J. H.; Osterwalder, J. ; Meier, F.; Bihlmayer, G.; Kane, C. L.; Hor, Y. S.; Cava, R. J.; Hasan, M. Z. Observation of Unconventional Quantum Spin Textures in Topological Insulators. *Science* **2009,** *323*, 919.

View Article Online
DOI: 10.1039/C7CP04875K

(7) Roy, R. Topological Phases and the Quantum Spin Hall Effect in Three Dimensions. *Phys. Rev. B* **2009**, *79,* 195322.

(8) Hsieh, D. ; Xia, Y.; Qian, D.; Wray, L.; Dil, J. H.; Meier, F.; Osterwalder, J.; Patthey, L.; Checkelsky, J. G.; Ong, N. P.; Fedorov, A.V.; Lin, H.; Bansil, A.; Grauer, D. ; Hor, Y. S.; Cava, R. J.; Hasan, M. Z. A tunable topological insulator in the spin helical Dirac transport regime. *Nature* **2009**, *460*,1101.

(9) Sánchez-Barriga, J.; Varykhalov, A.; Braun, J.; Xu, S.-Y.; Alidoust, N.; Kornilov, O.; Minár, J.; Hummer, K.; Springholz, G.; Bauer, G.; *et al.* Photoemission of Bi_2Se_3 with Circularly Polarized Light: Probe of Spin Polarization or Means for Spin Manipulation?. *Phys. Rev. X* **2014**, *4*, 011046.

(10) Sánchez-Barriga J.; Golias E.; Varykhalov A.; Kornilov O.; Braun J.; Yashina L.V.; Schumann R.; Minár J.; Ebert H.; Rader O; Ultrafast spin-polarization control of Dirac fermions in topological insulators. *Physical Review B* **2016**, 93, 155426.

(11) Honolka, J.; Khajetoorians, A. A.; Sessi, V.; Wehling, T. O.; Stepanow, S.; Mi, J.-L.; Iversen, B. B.; Schlenk, T.; Wiebe, J.; Brookes, N. B.; *et al.* In-Plane Magnetic Anisotropy of Fe Atoms on Bi_2Se_3 (111). *Phys. Rev. Lett.* **2012**, *108*.

(12) Scholz, M. R.; Sánchez-Barriga, J.; Marchenko, D.; Varykhalov, A.; Volykhov, A.; Yashina, L. V.; Rader, O. Intact Dirac Cone of Bi_2Te_3 Covered with a Monolayer Fe. *Phys. Status Solidi RRL - Rapid Res. Lett.* **2013**, *7*, 139–141.

(13) Shelford, L. R.; Hesjedal, T.; Collins-McIntyre, L.; Dhesi, S. S.; Maccherozzi, F.; van der Laan, G. Electronic Structure of Fe and Co Magnetic Adatoms on Bi_2Te_3 Surfaces. *Phys. Rev. B* **2012**, *86*,081304.

(14) Li, Z. L.; Yang, J. H.; Chen, G. H.; Whangbo, M.-H.; Xiang, H. J.; Gong, X. G. Strong Single-Ion Anisotropy and Anisotropic Interactions of Magnetic Adatoms Induced by Topological Surface States. *Phys. Rev. B* **2012**, *85*, 054426.

(15) West, D.; Sun, Y. Y.; Zhang, S. B.; Zhang, T.; Ma, X.; Cheng, P.; Zhang, Y. Y.; Chen, X.; Jia, J. F.; Xue, Q. K. Identification of Magnetic Dopants on the Surfaces of Topological Insulators: Experiment and Theory for Fe on Bi_2Te_3 (111). *Phys. Rev. B* **2012**, *85*, 081305.

(16) Eelbo, T.; Waśniowska, M. ; Sikora, M.; Dobrzański, M.; Kozłowski, A.; Pulkin, A.; Autès, G.; Miotkowski, I.; Yazyev, O. V. ; Wiesendanger, R. Strong out-of-plane magnetic anisotropy of Fe adatoms on Bi_2Te_3. *Phys. Rev. B* **2014,** *89*, 104424.

(17) Waśniowska, M.; Sikora, M. ; Dobrzański, M. ; Eelbo, T.; Soares, M. M.; Rams, M.; Miotkowski, I.; Wiesendanger, R.; Berndt, R.; Kąkol, Z.; Kozłowski, A. Investigating the differences between Co adatoms states on surfaces of selected bismuth chalcogenides. Phys. Rev. B **2015**, *92*, 115412.

(18) Schlenk, T.; Bianchi, M.; Koleini, M.; Eich, A.; Pietzsch, O.; Wehling, T. O.; Frauenheim, T.; Balatsky, A.; Mi, J.-L.; Iversen, B. B.; *et al.* Controllable Magnetic Doping of the Surface State of a Topological Insulator. *Phys. Rev. Lett.* **2013**, *110*, 126804.

(19) Polyakov, A.; Meyerheim, H. L.; Crozier, E. D.; Gordon, R. A.; Mohseni, K.; Roy, S.; Ernst, A.; Vergniory, M. G.; Zubizarreta, X.; Otrokov, M. M.; *et al.* Surface Alloying and Iron Selenide Formation in Fe/Bi_2Se_3 (0001) Observed by X-Ray Absorption Fine Structure Experiments. *Phys. Rev. B* **2015**, *92*, 045423.

(20) Vobornik, I.; Panaccione, G.; Fujii, J.; Zhu, Z.-H.; Offi, F.; Salles, B. R.; Borgatti, F.; Torelli, P.; Rueff, J. P.; Ceolin, D.; et al. Observation of Distinct Bulk and Surface Chemical Environments in a Topological Insulator under Magnetic Doping. *J. Phys. Chem. C* **2014**, *118*, 12333–12339.

(21) Mellnik, R.; Lee, J. S.; Richardella, A.; Grab, J. L.; Mintun, P. J.; Fischer, M. H.; Vaezi, A.; Manchon, A.; Kim, E.-A.; Samarth, N.; Ralph, D. C. Spin-transfer torque generated by a topological insulator. *Nature* **2014**, *511*, 449-451.

(22) Ivana Vobornik I.;, Manju, U; Fujii, J.; Borgatti, F; Torelli, P.; Krizmancic, D; Hor, Y. S.; Cava, R. J.; Panaccione, I.; Magnetic Proximity Effect as a Pathway to Spintronic Applications of Topological Insulators. *Nano Lett.* **2011**, *11*, 4079–4082.

(23) Li, J. ; Wang, Z. Y.; Tan, A.; Glans, P.-A.; Arenholz, E.; Hwang, C.; Shi, J.; Qiu, Z. Q. Magnetic dead layer at the interface between a Co film and the topological insulator Bi_2Se_3. *Phys. Rev. B* **2012**, *86*, 054430.

View Article Online
DOI: 10.1039/C7CP04875K

(24) Roushan, P.; Seo, J; Parker, C. V.; Hor, Y. S.; Hsieh, D.; Qian, D.; Richardella, A.; Hasan, M. Z.; Cava, R. J.; Yazdani, A. Topological Surface States Protected From Backscattering by Chiral Spin Texture. *Nature* **2009**, *460*, 1106-1109.

(25) Sánchez-Barriga J.; Varykhalov A.; Springholz G.; Steiner H.; Kirchschlager R.; Bauer G.; Caha O.; Schierle E.; Weschke E.; Ünal A.A.; Valencia S.; Dunst M.; Braun J.; Ebert H.; Minár J.; Golias E.; Yashina L.; Ney A.; Holy V.; Rader O. Nonmagnetic band gap at the Dirac point of the magnetic topological insulator $(Bi_{1-x}Mn_x)_2Se_3$. *Nat. Commun.* **2016**, *7*, 10559.

(26) Chen, T.; Liu, W.; Zheng, F.; Gao, M.; Pan, X.; van der Laan, G.; Wang, X.; Zhang, Q.; Song, F.; Wang, B.; Wang, B.; Xu, Y.; Wang, G;. Zhang, R. High-Mobility Sm-Doped Bi_2Se_3 Ferromagnetic Topological Insulators and Robust Exchange Coupling. Adv. Mater. **2015**, *27*, 4823–4829.

(27) Niu, W.; Du, K.; Wang, S.; Zhang, M.; Gao, M.; Chen, Y.; Liu, H.; Zhou, W.; Song, F.; Wang, P.; Xu, Y.; Wang, X.; Shen, J.; Zhang, R. Intrinsic ferromagnetism and quantum transport transition in individual Fe-doped Bi_2Se_3 topological insulator nanowires. Nanoscale **2017**, *9*, 12372.

(28) Chen, Y. L. ; Chu, J.-H.; Analytis, J. G.; Liu, Z. K.; Igarashi, K.; Kuo, H.-H.; Qi, X. L.; Mo, S. K.; Moore, R. G.; Lu, D. H.; *et al*. Massive Dirac fermion on the surface of a magnetically doped topological insulator. *Science* **2010**, *329*, 659-662.

(29) Schmidt, T. M.; Miwa, R. H.; Fazzio, A. Spin texture and magnetic anisotropy of Co impurities in Bi_2Se_3 topological insulators. *Phys. Rev. B* **2011**, *84*, 245418.

(30) Henk, J.; Flieger, M; Maznichenko I. V.; Mertig, I; Ernst, A.; Eremeev, S. V.; Chulkov, E. V. Topological character and magnetism of the Dirac state in Mn-doped Bi_2Te_3. *Phys. Rev. Lett.* **2012**, *109*, 076801.

(31) Henk, J.; Ernst, A.; Eremeev, S. V.; Chulkov, E. V.; Maznichenko, I. V.; Mertig, I. Complex Spin Texture in the Pure and Mn-Doped Topological Insulator Bi_2Te_3. *Phys. Rev. Lett.* **2012**, *108*, 206801.

(32) Abdalla, L. B.; Seixas, L.; Schmidt, T. M.; Miwa, R. H.; Fazzio, A. Topological insulator Bi_2Se_3(111) surface doped with transition metals: an ab-initio investigation. *Phys. Rev. B* **2013**, *88*, 045312.

(33) Chen, T.; Chen, Q.; Schouteden, K.; Huang, W.; Wang, X.; Li, Z.; Miao, F.; Wang, X.; Li, Z.; Zhao, B.; Li, S.; Song, F.; Wang, J.; Wang, B.; Van Haesendonck, C.; Wang, G. Topological transport and atomic tunnelling–clustering dynamics for aged Cu-doped Bi_2Te_3 crystals. Nature Commun. **2014**, *5*, 5022.

(34) Sánchez-Barriga, J.; Fink, J.; Boni, V.; Di Marco, I.; Braun, J. ; Minár, J.; Varykhalov, A.; Rader, O.; Bellini, V.; Manghi, F.; Ebert, H.; Katsnelson, M. I.; Lichtenstein, A. I.; Eriksson, O.; Eberhardt, W.; Dürr, H. A. Strength of Correlation Effects in the Electronic Structure of Iron. *Phys. Rev. Lett.* **2009**, *103*, 267203.

(35) Sánchez-Barriga, J.; Minár, J. ; Braun, J. ; Varykhalov, A.; Boni, V. ; Di Marco, I. ; Rader, O. ; Bellini, V.; Manghi, F.; Ebert, H.; Katsnelson, M. I.; Lichtenstein, A. I.; Eriksson, O.; Eberhardt, W.; Dürr, H. A.; Fink, J. Quantitative determination of spin-dependent quasiparticle lifetimes and electronic correlations in hcp cobalt. *Phys. Rev. B* **2010**, *82*, 104414.

(36) Sánchez-Barriga, J.; Braun, J. ; Minár, J. ; Di Marco, I. ; Varykhalov, A.; Rader, O.; Boni, V.; Bellini, V. ; Manghi, F.; Ebert, H.; Katsnelson, M. I.; Lichtenstein, A. I.; Eriksson, O. ; Eberhardt, W.; Dürr, H. A.; Fink, J. Effects of spin-dependent quasiparticle renormalization in Fe, Co, and Ni photoemission spectra: An experimental and theoretical study. *Phys. Rev. B* **2012**, *85*, 205109.

(37) Song, C.-L.; Jiang, Y.-P.; Wang, Y.-L.; Li, Z.; Wang, L.; He, K.; Chen, X.; Ma, X.-C.; Xue, Q.-K. Gating the Charge State of Single Fe Dopants in the Topological Insulator Bi_2Se_3 with a Scanning Tunneling Microscope. *Phys. Rev. B* **2012**, *86*, 045441.

(38) Kim, M.; Song, J.-H. Theoretical Investigation on the Magnetic Phase Stability of Fe-Doped Bi Tellurides. *J. Appl. Phys.* **2012**, *111*, 07E307.

(39) Fadley, C. S. Diffraction and Holography with Photoelectrons and Auger Electrons: Some New Directions. *Surf. Sci. Rep.* **1993**, *19*, 231–264.

(40) Matsushita, T.; Matsui, F.; Daimon, H.; Hayashi, K. Photoelectron Holography with Improved Image Reconstruction. *J. Electron Spectrosc. Relat. Phenom.* **2010**, *178–179*, 195–220.

View Article Online
DOI: 10.1039/C7CP04875K

(41) Kuznetsov M.V.; Yashina L.V.; Sánchez-Barriga J.; Ogorodnikov I. I.; Vorokh A. S.; Volykhov A.A.; Koch R. J.; Neudachina V.S.; Tamm M.E.; Sirotina A.P.; Varykhalov A.; Springholz G; Bauer G.; Riley J. D.; Rader O. Atomic structure of Bi_2Se_3 and Bi_2Te_3 (111) surfaces probed by photoelectron diffraction and holography**.** *Phys. Rev. B* **2015**, *91*, 085402.

(42) Scholz, M. R.; Sánchez-Barriga, J.; Marchenko, D.; Varykhalov, A.; Volykhov, A.; Yashina, L. V.; Rader, O. Tolerance of Topological Surface States towards Magnetic Moments: Fe on Bi_2Se_3. *Phys. Rev. Lett.* **2012**, *108*, 256810.

(43) Rosenberg, G.; Franz, M. Surface magnetic ordering in topological insulators with bulk magnetic dopants. *Phys. Rev. B* **2012**, *85*, 195119.

(44) Jiang, Y.; Wang, Y.; Sagendorf, J.; West, D.; Kou, X.; Wei, X.; He, L.; Wang, K. L.; Zhang, S.; Zhang, Z. Direct Atom-by-Atom Chemical Identification of Nanostructures and Defects of Topological Insulators. *Nano Lett.* **2013**, *13*, 2851–2856.

(45) Shtanov, V. I.; Yashina, L. V. On the Bridgman Growth of Lead–tin Selenide Crystals with Uniform Tin Distribution. *J. Cryst. Growth* **2009**, *311*, 3257–3264.

(46) Cousland, G. P.; Smith, A. E.; Riley, J. D.; Stampfl, A. P. J. Low Energy Photoelectron Diffraction Analysis at High Angular Resolution of Cu and Mn/Cu Surfaces. *J. Appl. Phys.* **2009**, *106*, 93510.

(47) García de Abajo, F. J.; Van Hove, M. A.; Fadley, C. S. Multiple Scattering of Electrons in Solids and Molecules: A Cluster-Model Approach. *Phys. Rev. B* **2001**, *63*, 075404.

(48) Dunitz, J. D. *X-Ray Analysis and the Structure of Organic Molecules*, Second Edition, Verlag Helvetica Chimica Acta, Zürich, **1995.**

(49) Dippel, R.; Weiss, K.-U.; Schindler, K.-M.; Gardner, P.; Fritzsche, V.; Bradshaw, A. M.; Asensio, M. C.; Hu, X. M.; Woodruff, D. P.; González-Elipe, A. R. A Photoelectron Diffraction Study of the Structure of PF3 Adsorbed on Ni{in111}. *Chem. Phys. Lett.* **1992**, *199*, 625–630.

(50) Kresse, G.; Hafner, J. *Ab Initio* Molecular Dynamics for Liquid Metals. *Phys. Rev. B* **1993**, *47*, 558–561.

(51) Kresse, G.; Hafner, J. *Ab Initio* Molecular-Dynamics Simulation of the Liquid-Metal–amorphous-Semiconductor Transition in Germanium. *Phys. Rev. B* **1994**, *49*, 14251–14269.

(52) Yashina, L. V.; Zyubina, T. S.; Püttner, R.; Zyubin, A. S.; Shtanov, V. I.; Tikhonov, E. V. A Combined Photoelectron Spectroscopy and Ab Initio Study of the Adsorbate System O_2 /PbTe(001) and the Oxide Layer Growth Kinetics. *J. Phys. Chem. C* **2008**, *112*, 19995–20006.

View Article Online
DOI: 10.1039/C7CP04875K

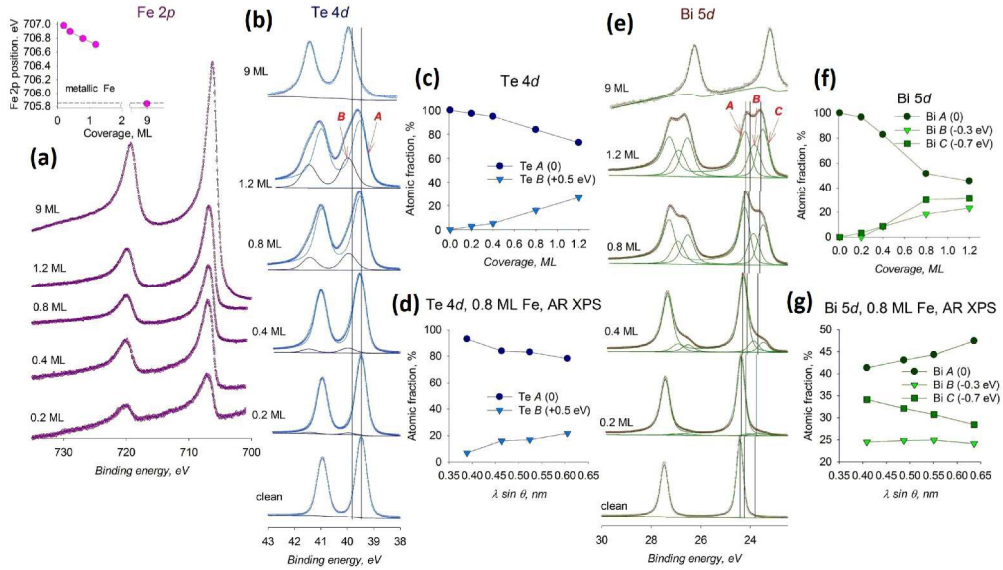

Fig. 1. Core-level photoemission spectra for the Fe-covered Bi2Te3 (111) surface. (a) Fe 2p and (b) Te 4d spectra as a function of Fe coverage measured with photon energies of hv=870 and 125 eV, respectively. (c) Relative intensity of spectral components measured as atomic fraction of the atom in the specific state in the Te 4d spectra shown in (b). (d) Corresponding angular dependence for an Fe coverage of 0.8 ML. (e) Similar measurements as in (b) for the Bi 5d core levels. (f) Relative intensity of the spectral components in the Bi 5d spectra shown in (e). (g) Angular dependence of the relative intensities of the Bi 5d spectral components after deposition of 0.8 ML Fe.

290x167mm (300 x 300 DPI)

View Article Online
DOI: 10.1039/C7CP04875K

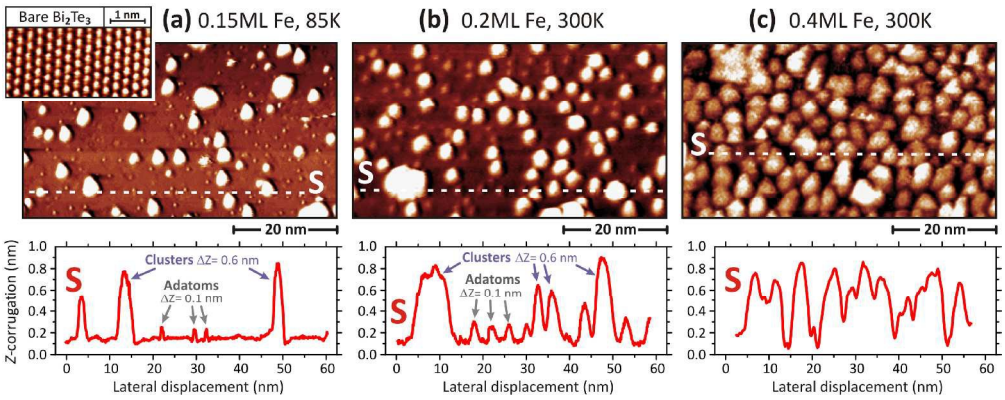

Fig. 2. STM images for the Fe-covered Bi2Te3 (111) surface. (a) 0.15 ML deposited at a temperature of 85 K. The inset shows the corresponding image of the clean Bi2Te3 surface with atomic resolution. STM images for (b) 0.2 ML Fe deposited at 300 K, and (c) 0.4 ML Fe deposited at 300K. The small Z-corrugation along the line scans marked by dashed lines in (a), (b) and (c) are given below each image.

285x111mm (300 x 300 DPI)

View Article Online
DOI: 10.1039/C7CP04875K

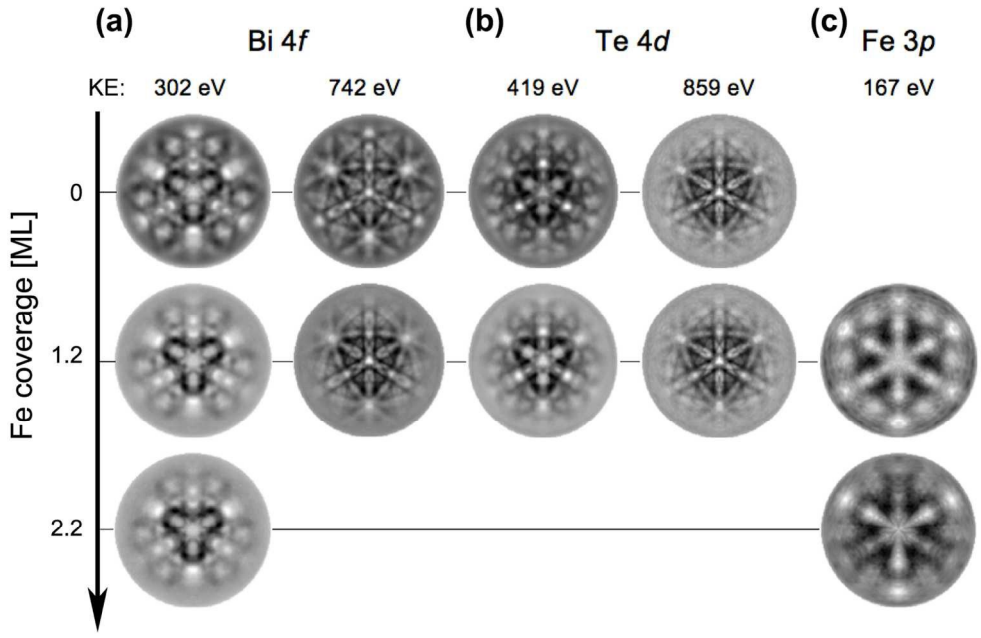

Fig. 3. Experimental photoelectron diffraction data for the Fe covered Bi2Te3 (111) surface. Diffraction patterns for (a) Bi 4f , (b) Te 4d and (c) Fe 3p core levels as a function of increasing Fe coverage, indicated as vertical axis (from top to bottom). The kinetic energy (KE) at which the patterns where recorded is indicated on top (from left to right).

176x112mm (300 x 300 DPI)

View Article Online
DOI: 10.1039/C7CP04875K

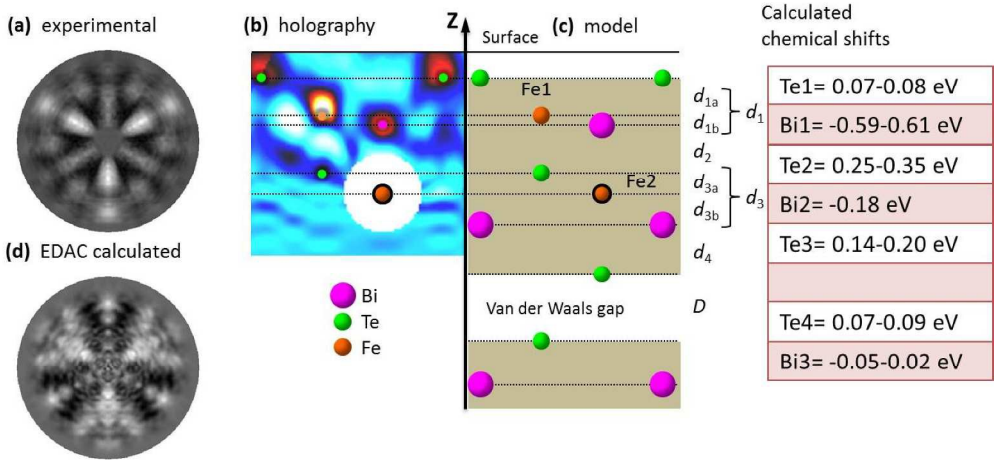

Fig. 4. Photoelectron diffraction experimental and theoretical results. (a) Fe 3p experimental diffraction pattern for 2.2 ML Fe on Bi2Te3. (b) Holography reconstruction of the Fe local environment. (c) Atomic model consistent with the results shown in (b). (d) Simulated core-level shifts for the different Te and Bi atoms in each layer obtained for the optimized structure with ¼ population of the position Fe 2. The spectral features Bi C and Bi B in Fig. 1 correspond to Bi1 and Bi2, respectively, while the spectral feature Te B to Te1+Te2+Te3 (not resolvable in the core-level spectra).

229x106mm (300 x 300 DPI)

View Article Online
DOI: 10.1039/C7CP04875K

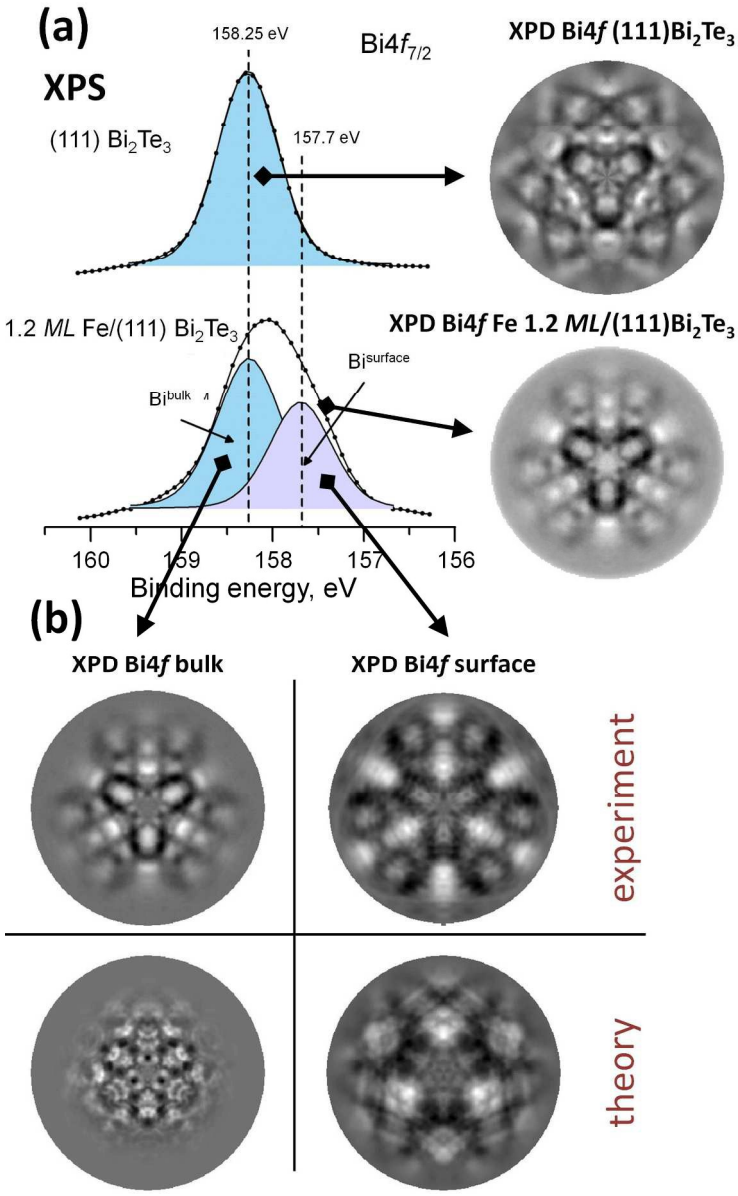

Fig. 5. Chemical state selective photoelectron diffraction. (a) Bi 4f7/2 spectra for clean Bi2Te3 surface (top) and after deposition of 1.2 ML Fe (bottom) and corresponding experimental diffraction patterns (right). (b) Experimental and EDAC simulated diffraction patterns for two different charge states of Bi, as decomposed in the spectrum for 1 ML Fe on Bi2Te3 in (a).

157x249mm (300 x 300 DPI)

View Article Online
DOI: 10.1039/C7CP04875K

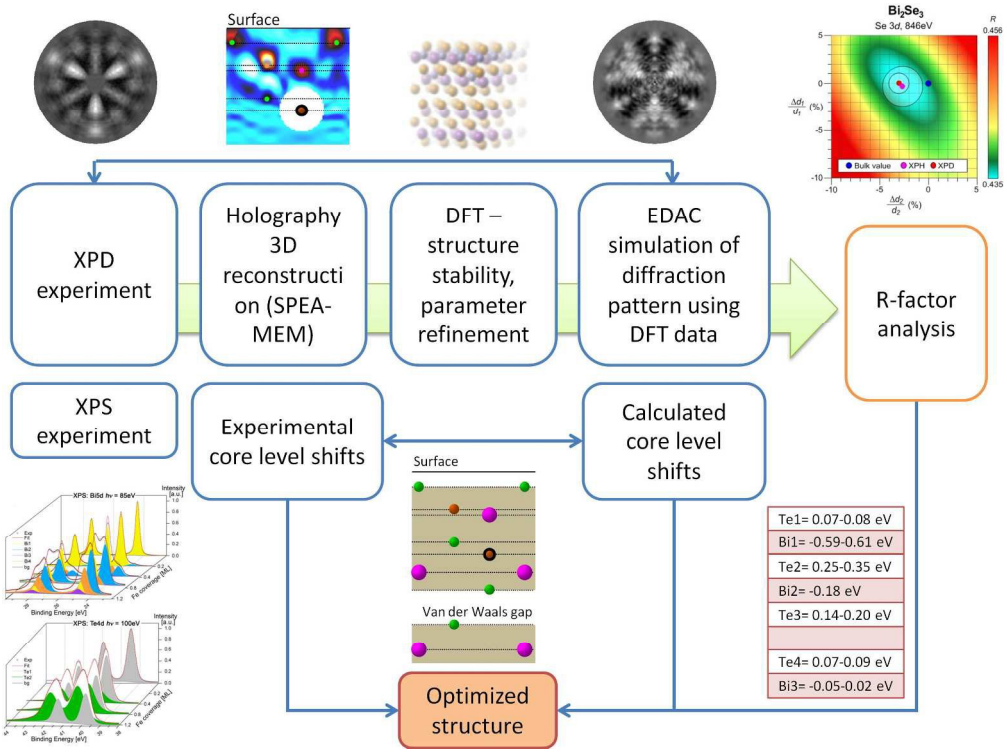

Fig. 6. Overview of the procedure used in the present work. The scheme illustrates a paradigm to determine the local structure of foreign atoms at the interface using full hemisphere photoelectron diffraction data.

242x180mm (300 x 300 DPI)

View Article Online
DOI: 10.1039/C7CP04875K

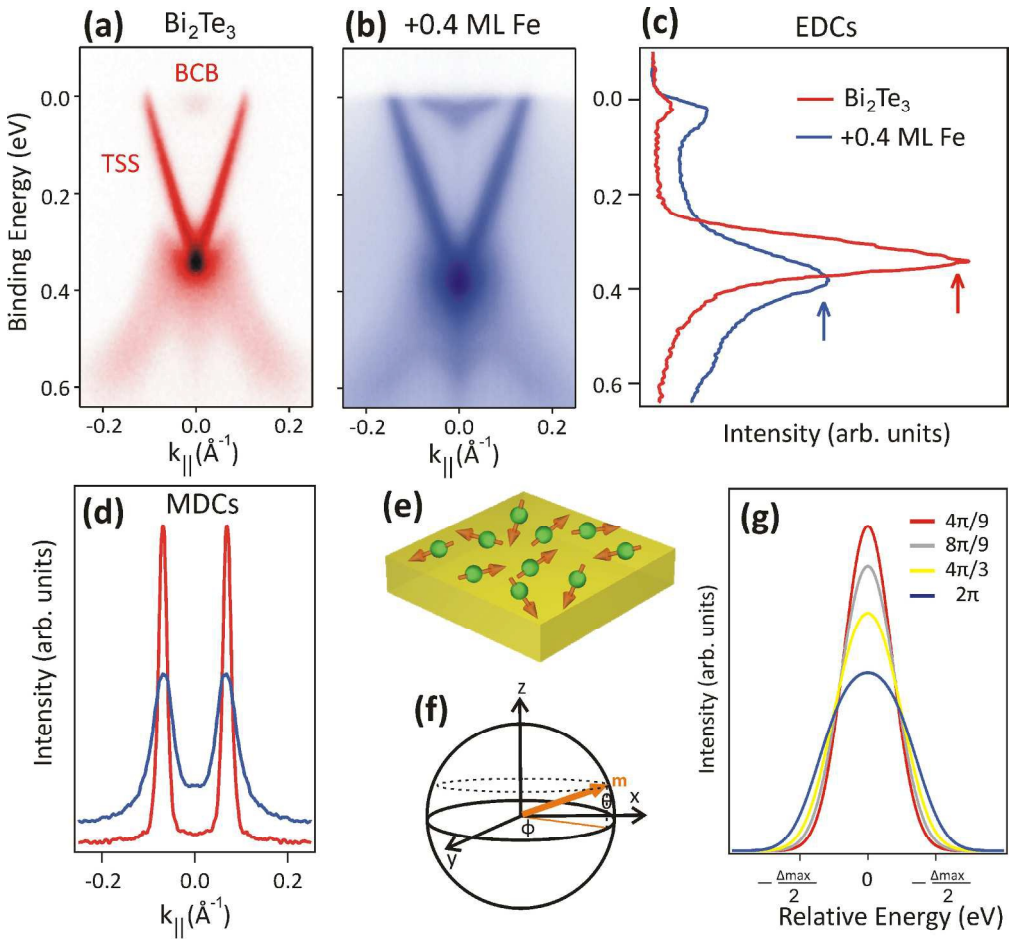

Fig. 7. Influence of Fe deposition on the electronic structure of Bi2Te3. (a) ARPES dispersion of clean Bi2Te3 measured at a photon energy of hv=55eV at room temperature. (b) Corresponding ARPES dispersion after deposition of 0.4 ML Fe. The intensity contribution from the bulk-conduction band (BCB) near the Fermi level and the TSS are clearly seen. (c) EDCs extracted from (a) and (b) at k||=0. (d) Corresponding MDCs extracted at 0.2 eV above the Dirac point. (e) Schematic of Bi2Te3 with Fe magnetic impurities on the surface. (f) Representation of Fe magnetic moment in three-dimensions. (g) Calculated spectral weight at the Dirac point for different constraints in the orientation of the Fe magnetic moments within a range of solid angles. The constraints correspond to symmetric polar angles below 45° with respect to the x-y plane, which add up to the total solid angle indicated in the legend.

205x191mm (300 x 300 DPI)

View Article Online
DOI: 10.1039/C7CP04875K

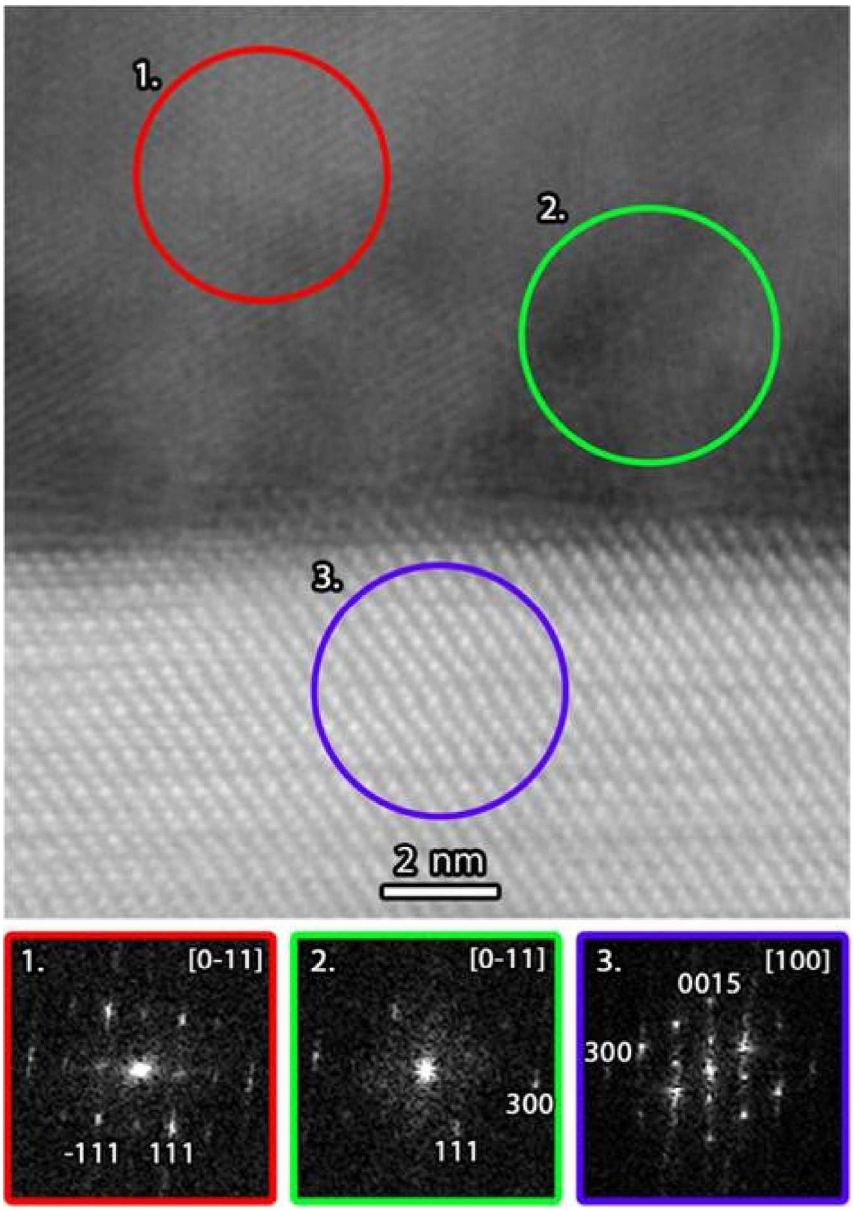

Fig. 8. Characterization of the interface structure for 20 nm thick Fe on Bi2Te3 using high-resolution STEM. (Top) Cross-sectional HAADF-STEM image. (Bottom) Corresponding Fourier transforms obtained from the green, blue and red regions labelled from 1 to 3, respectively.

158x224mm (300 x 300 DPI)

View Article Online
DOI: 10.1039/C7CP04875K

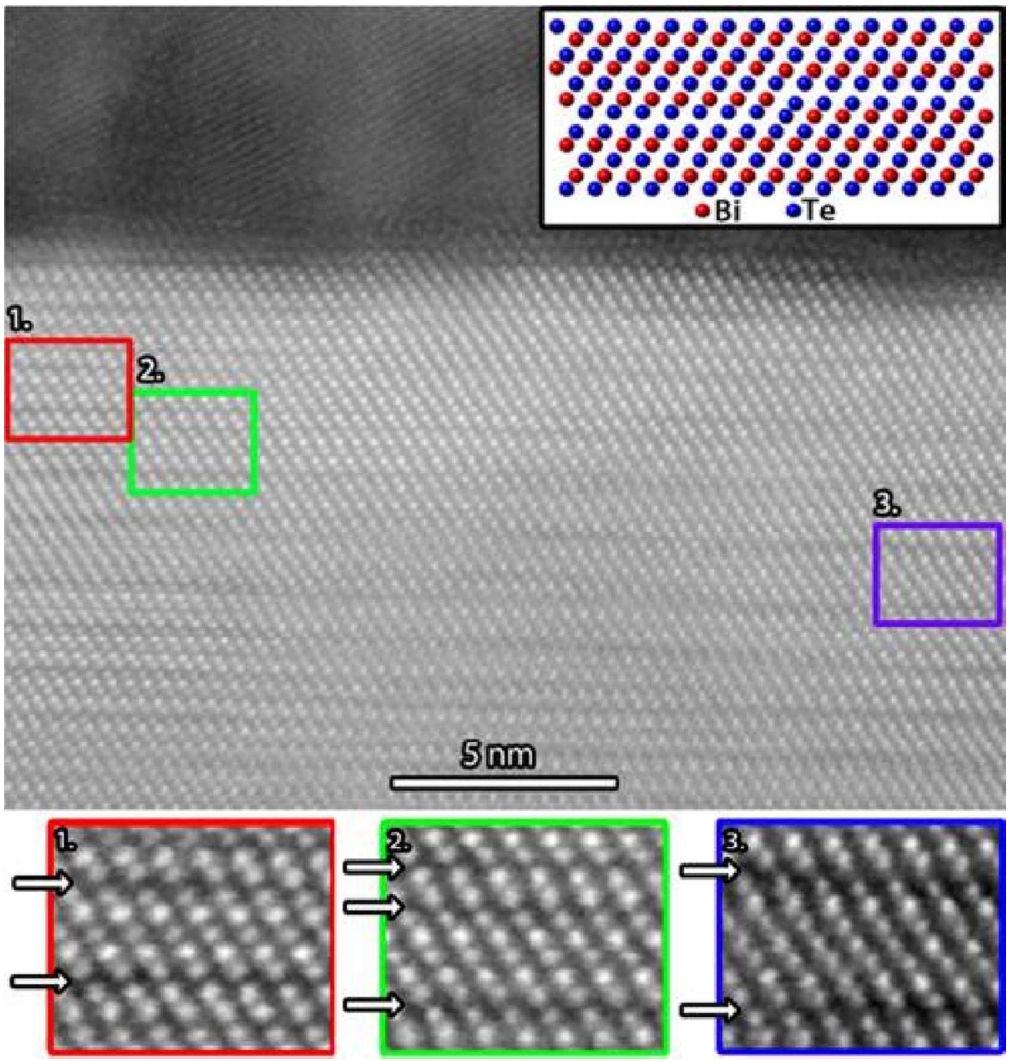

Fig. 9. Details on the interface structure of 20 nm Fe on Bi2Te3. The top Bi2Te3 layer is shown with enlargements of three indicated areas. Red (1): quintuple layer; green (2): quintuple layer with a double layer; blue (3): septuple layer. The arrows mark the Van der Waals gaps. The inset on the top right shows the transition from a quintuple layer to a septuple layer, using the model proposed in Ref. 41.

101x106mm (300 x 300 DPI)

View Article Online
DOI: 10.1039/C7CP04875K

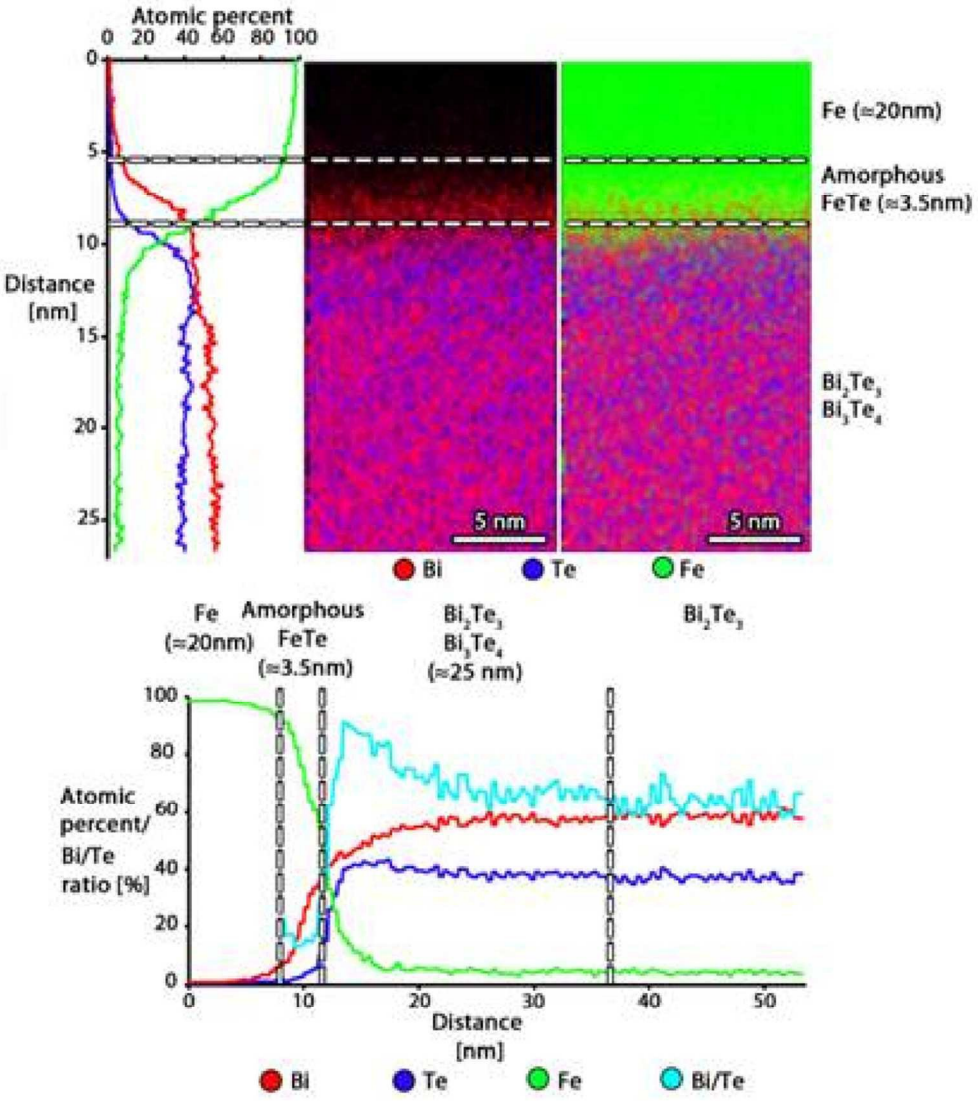

Fig. 10. Interface composition of 20 nm Fe on Bi2Te3. (Top) STEM–EDX maps and corresponding line profiles. (Bottom) Line profiles taken over a larger depth emphasize the deviation of the Bi:Te ratio in the top layer and the regularization of this ratio when going deeper into the bulk.

103x114mm (300 x 300 DPI)